



Thermal management of battery cell module using a hybrid nanofluid filled inverted right-angled porous triangular cavity through natural convection

A. Vanav Kumar¹ · Ali J. Chamkha² · Swapnali Doley¹ · L. Jino³ · Ashwin Jacob³ · E. Manoj³ · S. Arockia Suthan³ · A. Jayaganthan³

Received: 14 December 2023 / Accepted: 16 June 2024
© Akadémiai Kiadó, Budapest, Hungary 2024

Abstract

The study investigates the approach to enhance the thermal management of battery cell module by attaching number of inverted triangular cavity to its casing. A sinusoidal heating is considered to battery cell module or a left wall of the cavity. The sinusoidal heated region is considered to be a function of amplitude ratio. The objective is to transfer the heat from module using natural convection process. The enhanced heat transfer is possible by adopting hybrid nanofluid in a triangular cavity due to its improved thermophysical properties. Thus, the investigation on natural convection heat transfer, fluid flow, and irreversibility within an inverted right-angled triangular porous cavity is conducted. Numerical results are obtained through an own-house FORTRAN coding, that uses the streamfunction–vorticity algorithm. The numerical results are derived for various values with Rayleigh number ($10^3 - 10^6$), Darcy number ($10^{-5} - 10^{-1}$), Hartmann number ($0 - 50$), amplitude ratio ($0.0 - 0.9$) and volume fraction of nanoparticles ($0.01 - 0.04$), respectively. The irreversibility and flow results are compared with the various hybrid nanofluids. The study indicates that opting inverted right-angled triangular cavity rather than a square shape leads to an improvement in heat transfer. Accordingly, this inverted right-angled triangular cavity natural convective cooling can be considered as optimum design with the battery cell module for improved thermal management.

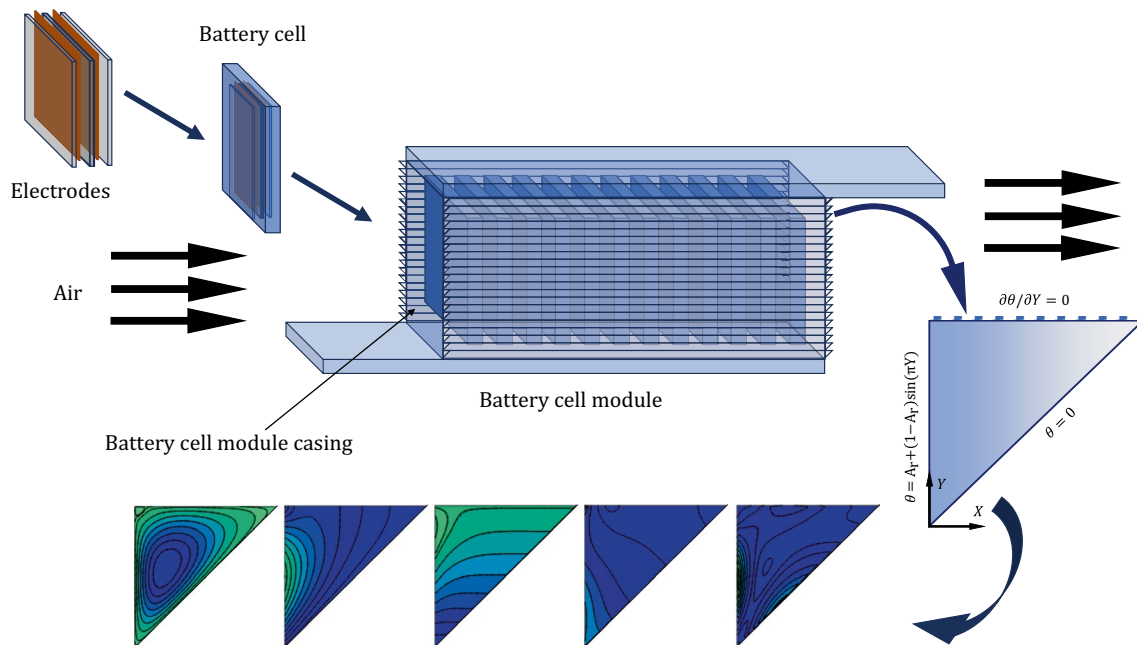
✉ L. Jino
jinogojulee@gmail.com

¹ Department of Basic and Applied Science, National Institute of Technology, Jote, Arunachal Pradesh, India

² Faculty of Mechanical Engineering, Kuwait College of Science and Technology, Doha, Kuwait

³ School of Mechanical Engineering, Sathyabama Institute of Science and Technology, Chennai, Tamil Nadu, India

Graphical abstract



Keywords Inverted triangle cavity · Hybrid nanofluid · Battery cell module · Heatlines · Entropy

Abbreviations

Parameters

A	Amplitude ratio
Be	Bejan number
c_p	Specific heat ($J\ Kg^{-1}\ K^{-1}$)
Da	Darcy Number
g	Gravity ($m\ s^{-2}$)
Ha	Hartmann number
k	Thermal conductivity ($W\ m^{-1}\ K^{-1}$)
Nu	Nusselt number
P, p	Pressure ($kg\ m^{-1}\ s^{-2}$)
Pr	Prandtl number
Ra	Rayleigh number
$S_\theta, S_{\theta T}$	Entropy generation by heat transfer
$S_\psi, S_{\psi T}$	Entropy generation by fluid friction
S_T	Total entropy generation
T	Dimensional temperature (K)
u	Horizontal velocity ($m\ s^{-1}$)
U	Dimensionless horizontal velocity
v	Vertical velocity (m/s)
V	Dimensionless vertical velocity
x	Horizontal direction (m)
X	Dimensionless horizontal direction
y	Vertical direction (m)
Y	Dimensionless vertical direction

Greek symbols

α	Thermal diffusivity ($m^2\ s^{-1}$)
β	Thermal expansion coefficient (K^{-1})
ϵ	Ratio due to irreversibility
ϕ	Solid volume fraction
\mathfrak{R}	Root mean square deviation
θ	Dimensionless temperature
Θ_{cup}	Cup-mixing temperature
μ	Dynamic viscosity ($Ns\ m^{-2}$)
ρ	Density ($kg\ m^{-3}$)
σ	Electrical conductivity ($S\ m^{-1}$)
ψ	Streamfunction
Π	Heatlines

Subscripts

fl	Base fluid
hn	Hybrid nanofluid
hp	Hybrid nanoparticle
p	Nanoparticle
h	Hot
c	Cold

Text abbreviations

Al_2O_3	Aluminum oxide
Ag	Silver
Cu	Copper
EV	Electric vehicle
FDM	Finite difference method

MHD	Magneto hydrodynamics
MWCNT	Multi-walled carbon nanotubes
NCF	Natural convection flow
TC	Triangular cavities
TiO ₂	Titanium oxide

Introduction

The depletion of petroleum fuels leads to the development of electric vehicles (EVs) to promote the sustainable transportation. In EV's, the batteries act as a superior power source. The need of thermal management of batteries has become very crucial to make electron transport efficient and to longevity. By interconnecting battery heat with the fluid dynamics probes, the potential way to the battery thermal management, particularly through convection. The study aims to utilize air around moving vehicles for cooling during natural convection process. The natural convection flow, driven by free energy gradients, leads to a significant role in energy extraction and has gained worldwide attention for its importance.

Research on free convection focuses on ordered molecular motion, also known as irreversibility analysis, helps in predicting useful work extracted during natural convection. Accordingly, the present study aims to examine irreversibility associated with heat transfer and fluid friction, along with heat and fluid flow patterns within an inverted triangular cavity integrated with the battery cell module casing. The similar thermal management studies on batteries using fluid dynamics have been initiated by various researchers [1–4], and this study advances heat transport through natural convection processes.

The naturally occurring energy flow associated with free convection pays a wide range of daily applications, namely, reservoirs, solar energy, cooling of electronic components, nuclear reactors, catalytic reactors, reactions of a chemical/biochemical reaction, etc. [5–7]. For example, the rotational flow of nanofluids during convection is utilized in biomedical engineering applications [8]. In early stages, the natural convection flow (NCF) within an equilateral triangular cavity (TC) was studied by Ribbens et al. [9]. Their study illustrated fluid flow structures using streamfunction and isotherm tools derived through finite difference discretization (FDD). Subsequently, Varol et al. [10] utilized the heatline tool to visualize the heat flow rather than the temperature distribution by isotherms. They utilized FDD-based solutions to examine NCF behavior in a sinusoidally bottom-heated TC. It was observed that NCF behavior improved with increasing Ra. Basak et al. [11] investigated the heat transfer within the inverted isosceles right-angled TC due to NCF using streamfunction, heatfunction and isotherms. Here, the triangle is heated

to both the inclined wall and cooled to the top wall. The NCF is more found in the lower Pr fluid than the higher Pr number fluid due to its viscous effect. In continuation to previous study, Kaluri et al. [12] considered the right angled TC to explore the NCF due to various combinations of thermal wall conditions. It is considered that the vertical and inclined walls are heated even, cooled even or heated linearly, while the bottom wall was treated as adiabatic. The NCF is examined for the various top angles, and it is found that the streamline circulation is more at higher top angles than the lower top angles.

The importance of porous medium on heat transfer process is due to its improved surface area within the area. In regard to this, various study was conducted to analysis, the heat transfer over the porous medium. For instance, Krishna et al. [13] investigated the heat transfer and natural convection flow (NCF) of a Jeffrey fluid over a vertical plate under porous medium conditions. Followed by this study, Krishna et al. [14, 15] further examined MHD free convective heat and mass transfer of micropolar/second-grade fluid past a plate/sheet under porous medium conditions. Additionally, Krishna et al. [16, 17] extended their study to investigate the effects of chemical reaction, Soret, Hall, and Joule effects on heat transfer and mass transfer rates when fluid flows past a porous plate. Besides this, Basak et al. [18] done the NCF analysis to porous right-angled isosceles TC with cooled top wall and heated remaining wall. It is noted that at larger values of Ra, the heat transfer is more for higher values of Darcy number. Yesiloz and Aydin [19] numerically and experimentally examined NCF due to bottom heating in a right-angled triangular cavity. They found that at higher values of Ra, the convection flow and corresponding heat transfer were significantly increased. Recently, Nazir et al. [20] studied the radiative-NCF under heat generation effects within the equilateral TC. They heated the left inclined wall while cooling the remaining walls and found that the streamfunction increased with augmentation of radiation, buoyancy effects, and permeability.

The analysis to limpidity of irreversibility due to fluid friction or heat transfer to convert into useful work by fluids can be investigated with the laws of thermodynamics. The entropy generation study is very important to the execution of entropy generation minimization. In regard to this, Varol et al. [21, 22] examined the production of entropy within the heated isosceles TC due to NCF. They considered the TC with the bottom partially and fully heated as well as sinusoidal heated isosceles TC with various angles of rotation. It is noted that the Bejan number decreases with the heater length at the bottom and for increasing the value of Ra. In addition, it is observed that the entropy generation has an impact with the rotation of TC. Basak et al. [23] analyzed the function of irreversibility while NCF. They

consider the right-angled TC with various thermal conditions such as constant heating, constant cooling linear heating and adiabatic, respectively. Bhardwaj et al. [24] studied the entropy generation during NCF within a porous wavy TC with a sinusoidally heated bottom wall. They observed that the Bejan number was low and the Nusselt number was high when the permeability of the TC was high. Biswal and Basak [25] briefly reviewed the nature of irreversibility during NCF on various shapes of cavities. The cavities with various shapes such as square, square-convex, square-concave, equilateral triangle, right-angled triangle, trapezoid, square-pot, and wavy respectively are considered with and without inclinations. Recently, Rashidi and Yang [26] utilized various cavity shapes to understand heat flow and entropy generation in different thermal solar systems. Their study reviewed thermal systems in terms of cavities with different shapes and noted that viscous irreversibility was high near boundaries exposed to the solar system.

The fluid flow nature with its own capability is induced by the addition of nanoparticles within the fluids [27]. Thus, the heat/fluid flow studies with incorporating nanofluids are improved periodically. In regard to this Buongiorno [28] investigated the slip mechanism that generates relative velocity between the nanoparticle and base conventional fluids. From the investigation, it is found that the thermophoresis and Brownian motion are the prime slip mechanism that has to be considered. Consequently, research based on nanofluids has increased significantly. The nanofluids are composed of nano-shaped particles, enhance the thermal conductivity of normal fluids, intensifying heat transfer, as discussed by Sheikholeslami and Ganji [29]. The heat transfer study by Krishna and Chamkha [30] is done between the two parallel disk filled with nanofluid under porous medium. It is found that the convection heat transfer improves with the nanofluid.

Apart from the heat transfer enhancement applications, the vast applications of nanofluids are found in the article by Wong and Leon [31]. The researchers used nanofluids to examine the heat transfer/fluid flow characteristics due to NCF within the cavity. For instance, Basak and Chamkha [32] examined the heat transfer rate of various nanofluids against the normal base fluid. For this analysis, the nanofluid is loaded within a square-shaped cavity and heated toward the left/bottom wall. The examination shows the enhancement of the Nusselt number during NCF of nanofluids. Sheremet and Pop [33] considered a porous, right-angled TC to analysis the NCF using Buongiorno's model. The flow within the TC is improved by enhancing the buoyancy effect and further leads to quantification of the heat transfer rate of nanofluid with respect to an increase in the value of Ra. More recently, Redouan et al. [34] examined the effects of MHD-NCF due to hot thermal boundary over the left/bottom wall and cool wavy long inclined wall of the right-angled porous TC. Moreover,

the rotating cylinder is bounded at the middle. The study shows that the average Nusselt number decreases until Ra reaches 10^5 and increases further.

Bondareva et al. [35] entertained partially opened TC to analysis the EG due to NCF with respect to partial heating at the bottom. The analysis denotes a huge drop in the average Bejan number while increasing the Ra from 10^4 to 10^5 and 10^6 . Also, a small rise in average Bejan number is noted while increasing the amount of volume fraction of nanoparticles. Al-Zamily [36] investigated the irreversibility of heat and fluid flow within a layered nanofluid-filled cavity due to NCF with respect to partially heated flux boundary at the left. One of the layers within the square cavity is porous and the remaining two layers are non-porous, respectively. Das et al. [37] conducted an extensive analysis of NCF within cavities of different shapes with or without a porous medium, filled with conventional or nanofluid, respectively. The study was further extended to examine entropy generation, showing that the cavity's inclination also contributes to reducing entropy generation.

Humic and Humic [38] reviewed entropy generation of hybrid/normal nanofluids during NCF, considering various cavity shapes with flux/even/partially heated thermal boundaries. Tayebi et al. [39] explored the entropy changes within an elliptical-shaped annulus with heated internal boundary and cooled external boundary, noting an improvement in the total entropy of CuAl_2O_3 -water hybrid nanofluid with the convection effects and addition of nanoparticles volume fraction during NCF. Recently, Kumar et al. [40] examined the irreversibility changes due to NCF within a cavity loaded with MWCNT-water nanofluid. The examination is done with a linear or even heated thermal boundary at the left. The main finding of the study is the Bejan/Nusselt number is higher for the even heated boundary than the linear heated one. Jino and Vanav [41] compared the heat transfer behavior of water-based Cu or Al_2O_3 or $\text{Cu-Al}_2\text{O}_3$ nanofluid due to MHD-NCF inside a porous enclosure allotted with sinusoidal boundary conditions. It is noted that the hybrid nanofluid heat transfer behavior is better than the normal nanofluid, mainly at the higher values of Ra and Da. Swamy et al. [42] analyzed irreversibility due to fluid friction/heat transfer in a Cu-water nanofluid-filled rectangular enclosure, observing that the enclosure's aspect ratio significantly influences total entropy generation and Bejan number.

The above-mentioned studies denote the importance of natural convection for the heat transfer applications, and the presence of nano-sized particles, either a single component or hybrid, enhances this heat transfer process within the base liquid solution. Various heat transfer studies have been conducted by various researchers with respect to different shapes of the cavity, and this current study considers the inverted right-angled TC for the better heat transfer process. The battery cell module comprises multiple battery cells, and

the heat has to be advected for better efficiency. In addition to the convective design [1–4] of a battery module, a series of right-angled triangular cavities that are inverted and filled with hybrid nanofluid (the thermophysical properties are included in the Table 1) are externally attached to the battery cell module casing. The inclined wall of the TC is exposed to the surrounding air for heat transfer enhancement process by using natural convection. Using a detailed examination of the free convection process within the TC using an entropy generation study, this research provides valuable insights for engineers to enhance the heat transfer process. Particularly, these findings contribute to better designs to engineers for the thermal management of EV batteries, which advances the sustainable transport.

In summary, the key objectives of the study are,

1. To improve the thermal management of battery cell module by using air around moving vehicles for cooling during the natural convection process.
2. For the thermal management, series of cavities are attached to the battery cell module casing and to analysis the heat transfer and entropy generation within a cavity (filled with hybrid nanofluid) due to free convection.

Mathematical modeling of a problem

To analysis the flow irreversibility within an inverted right-angled TC, mathematically the coordinates are outlined at $(0,0)$, $(0,y)$ and (x,y) . Here, the left vertical wall of the TC is managed with sinusoidally heated and the heating intensity is a function of amplitude ratio A_r . Non-dimensionally, the temperature distribution at a left wall is given as $\theta = A_r + (1 - A_r)\sin(\pi Y)$. Aside from the left wall, the top wall of the inverted TC is natured as adiabatic and the inclined wall is considered as low thermal temperature. Non-dimensionally it is denoted by $\partial\theta/\partial Y = 0$ and $\theta = 0$ as shown in Fig. 1. Other than the thermal boundaries, the velocities at the walls are considered as no-slip effects (i.e., all the velocities at the fixed walls are zero).

Inside the inverted porous right-angled TC, one of the hybrid nanofluids, such as Cu–Ag–water, Cu– Al_2O_3 –water, Cu–MWCNT–water or Cu– TiO_2 –water, is provided. Inside the cavity, the entropy analysis to be done along with the

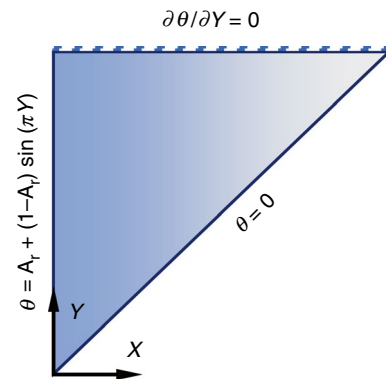


Fig. 1 Physical domain

NCF examination. To achieve this, the necessary governing equations are derived to examine the heat and fluid flow patterns within an inverted triangular cavity integrated with the battery cell module casing, under the following approximations and assumptions:

- The number of inverted right-angled triangle cavities are attached externally to the battery cell module casing. The battery has no contact with the inner side of the casing or battery cell module or the series of TC.
- The free convection flow simulations of a cavity are considered to two dimensions in space (X and Y axes direction) only.
- The hybrid nanofluid is incompressible in nature and considered laminar.
- The Boussinesq approximations are considered to derive ruling equations.
- No-slip conditions are valid (i.e., all the velocities are zero at the fixed walls).
- The effects such as Hall current, electrical resistance heating, ion slip, viscous dissipation, heat generation and radiation are not included in the study.
- Applied magnetic field effect is considered by neglecting the induced magnetic field.
- The water and hybrid nanoparticles are considered to be no-slip and in thermally equilibrium.
- All individual nanoparticles are assumed to be similar in shape (spherical).

Table 1 Various thermophysical properties of nanoparticle and water solution

	Water	MWCNT	Al_2O_3	Cu	TiO_2	Ag
$\rho/\text{kg m}^{-3}$	997.1	1600	3970	8933	4250	10,500
$C_p/\text{J Kg}^{-1} \text{K}^{-1}$	4179	796	765	385	686.2	235
$k/\text{W m}^{-1} \text{K}^{-1}$	0.613	3000	40	401	8.9528	429
$\beta/\text{K}^{-1} \times 10^{-5}$	21	2.0	0.85	1.67	0.9	1.89
$\sigma/\text{S m}^{-1}$	0.05	4.8×10^{-7}	10^{-10}	5.96×10^7	0.24×10^7	6.3×10^7

- The flow of hybrid nanofluid is considered as single-phase fluid.

With the assumptions, the governing equations are derived and written non-dimensionally as [37, 43–45],

$$\frac{\partial U}{\partial X} + \frac{\partial V}{\partial Y} = 0 \tag{1}$$

$$U \frac{\partial U}{\partial X} + V \frac{\partial U}{\partial Y} + \frac{\mu_{hn}}{\rho_{hn} \alpha_{fl}} \frac{U}{Da} = \frac{\mu_{hn}}{\rho_{hn} \alpha_{fl}} \left(\frac{\partial^2 U}{\partial X^2} + \frac{\partial^2 U}{\partial Y^2} \right) - \frac{\partial P}{\partial X} \tag{2}$$

$$U \frac{\partial V}{\partial X} + V \frac{\partial V}{\partial Y} + \frac{\mu_{hn}}{\rho_{hn} \alpha_{fl}} \frac{V}{Da} = \frac{\mu_{hn}}{\rho_{hn} \alpha_{fl}} \left(\frac{\partial^2 V}{\partial X^2} + \frac{\partial^2 V}{\partial Y^2} \right) - \frac{\partial P}{\partial Y} + \frac{(\rho\beta)_{hn}}{\rho_{hn} \beta_{fl}} Ra Pr(\theta) - \frac{\rho_{fl} \sigma_{hn}}{\rho_{hn} \sigma_{fl}} Ha^2 Pr(V) \tag{3}$$

$$U \frac{\partial \theta}{\partial X} + V \frac{\partial \theta}{\partial Y} = \frac{\alpha_{hn}}{\alpha_{fl}} \left(\frac{\partial^2 \theta}{\partial X^2} + \frac{\partial^2 \theta}{\partial Y^2} \right) \tag{4}$$

The above equations signify the two-dimensional continuity or mass conservation (Eq. 1), X and Y directional momentum conservation (Eq. 2) and temperature or energy equation (Eq. 3), respectively. The parameters such as density, heat capacity, viscosity, thermal conductivity and thermal expansion co-efficient of a hybrid nanofluid and these parameters relays on the properties of an individual nanoparticle (Cu, Ag, Al₂O₃, MWCNT and TiO₂ nanoparticles) and base fluid (water) such as,

$$\rho_{hn} = \rho_{fl} - \rho_{fl} \sum \phi_i + \rho_{hp} \sum \phi_i \tag{5}$$

$$(\rho c_p)_{hn} = (\rho c_p)_{fl} - (\rho c_p)_{fl} \sum \phi_i + (\rho c_p)_{hp} \sum \phi_i \tag{6}$$

$$\mu_{hn} = \mu_{fl} / \left(1 - \sum \phi_i \right)^{2.5} \tag{7}$$

$$k_{hn} = \left[k_{fl} \left(k_{hp} + 2k_{fl} - 2k_{fl} \sum \phi_i + 2k_{hp} \sum \phi_i \right) \times \left(k_{hp} + 2k_{fl} - k_{fl} \sum \phi_i + k_{hp} \sum \phi_i \right)^{-1} \right] \tag{8}$$

$$(\rho\beta)_{hn} = (\rho\beta)_{fl} - (\rho\beta)_{fl} \sum \phi_i + (\rho\beta)_{hp} \sum \phi_i \tag{9}$$

Moreover, other parameters used for non-dimensionalizing Eqs. (1–4) are:

$$U = uH/\alpha_{fl} \tag{10}$$

$$V = vH/\alpha_{fl} \tag{11}$$

$$X = x/H \tag{12}$$

$$Y = y/H \tag{13}$$

$$P = \rho H^2 / \rho_{hn} \alpha_{fl}^2 \tag{14}$$

$$\theta = (T - T_c) / \Delta T \tag{15}$$

$$Ra = ((T - T_c) \beta_{fl} g H^3) / (v_{fl} \alpha_{fl}) \tag{16}$$

$$Da = K/H^2 \tag{17}$$

$$Ha = \sqrt{\sigma_{fl} / \rho_{fl} v_{fl}} (BH) \tag{18}$$

$$Pr = v_{fl} / \alpha_{fl} \tag{19}$$

$$\alpha_{hn} = k_{hn} / (\rho c_p)_{hn} \tag{20}$$

Here, U, V, θ, P are the dimensionless velocities, temperature and pressure with respect to the direction X and Y , respectively. Moreover, Ra, Da, Ha and Pr represents the Rayleigh number (convection parameter), Darcy number (Permeability parameter), Hartmann number (Magnetic parameter) and Prandtl number (property of fluid). In addition, the subscripts fl represents base fluid and hp represents the contribution of nanoparticle 1 and nanoparticle 2. The mixture property of hybrid nanoparticle is given by,

$$\rho_{hp} = \frac{\sum (\phi)_i (\rho)_i}{\sum \phi_i} \tag{21}$$

$$\beta_{hp} = \frac{\sum (\phi)_i (\beta)_i}{\sum \phi_i} \tag{22}$$

$$k_{hp} = \frac{\sum (\phi)_i (k)_i}{\sum \phi_i} \tag{23}$$

$$(c_p)_{hp} = \frac{\sum (\phi)_i (c_p)_i}{\sum \phi_i} \tag{24}$$

The Eqs. (1)–(5) are utilized to calculate the required flow fields under the following boundary conditions on three walls of the cavity as [46],

At left wall:

$$\theta = A_r + (1 - A_r)\sin(\pi Y), U = 0, V = 0 \tag{25}$$

At top wall:

$$\partial\theta/\partial Y = 0, U = 0, V = 0 \tag{26}$$

At inclined wall:

$$\theta = 0, U = 0, V = 0 \tag{27}$$

After the flow solutions are derived, the entropy or irreversibility due to velocity gradient/heat transfer (S_ψ/S_θ) to be derived. Thus, irreversibility is calculated using the velocity and temperature gradient as [37, 47, 48],

$$S_\psi = \epsilon \frac{\mu_{hn}}{\mu_f} \left[\frac{1}{Da} (U^2 + V^2) + \left\{ 2 \left(\left(\frac{\partial U}{\partial x} \right)^2 + \left(\frac{\partial V}{\partial y} \right)^2 \right) + \left(\frac{\partial U}{\partial Y} + \frac{\partial V}{\partial X} \right)^2 \right\} \right] + \epsilon \frac{\sigma_{hn}}{\sigma_f} Ha^2 V^2 \tag{28}$$

$$S_\theta = \frac{k_{hn}}{k_f} \left[\left(\frac{\partial \theta}{\partial x} \right)^2 + \left(\frac{\partial \theta}{\partial y} \right)^2 \right] \tag{29}$$

Here, the irreversibility ratio can be taken between $10^{-4} \leq \epsilon \leq 10^{-2}$.

On integration to the above parameter toward both directions provides the total entropy or irreversibility due to velocity gradient/heat transfer ($S_{\psi T}/S_{\theta T}$).

$$S_{\theta T} = \int S_\theta dXdY \tag{30}$$

$$S_{\psi T} = \int S_\psi dXdY \tag{31}$$

In addition to the above, the overall entropy or irreversibility (S_T) due to velocity gradient and heat transfer within the TC due to natural/free convection is given by,

$$S_T = S_{\theta T} + S_{\psi T} \tag{32}$$

In the case of natural convection flow (NCF) within a porous triangular cavity (TC), there must be a dominance of any mode of heat transfer, such as conduction and convection. This can be determined by employing a non-dimensional parameter known as the Bejan number (Be). The Bejan number is defined as the ratio of total entropy or irreversibility due to heat transfer to the total entropy or irreversibility due to the combined velocity gradient and heat transfer.

$$Be = \frac{S_{\theta T}}{S_T} \tag{33}$$

Further, the thermal mixing rate, heat transfer rate and temperature uniformity within the cavity can be defined

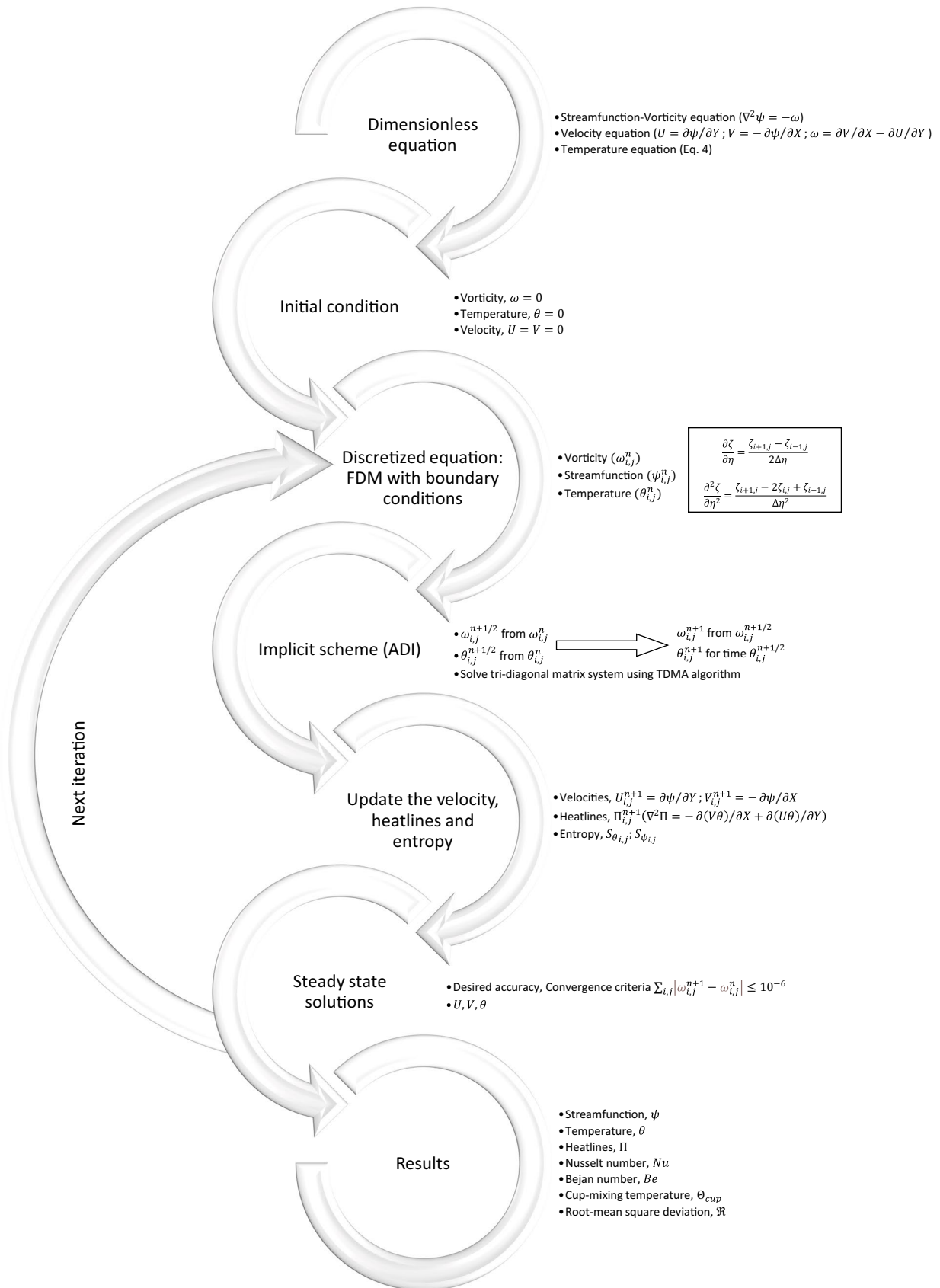
using cup-mixing temperature (Θ_{cup}), Nusselt number (Nu) and root-mean-square deviation (\mathfrak{R}), respectively [43].

$$\Theta_{cup} = \frac{\int \int \hat{V}(X, Y)\theta(X, Y)dXdY}{\int \int \hat{V}(X, Y)dXdY} \tag{34}$$

$$Nu = -\frac{k_n}{k_f} \int \left(\frac{\partial \theta}{\partial Y} \right)_{Y=0} dX \tag{35}$$

$$\mathfrak{R} = \sqrt{\frac{\sum_{i=1}^N (\theta - \Theta_{cup})^2}{N}} \tag{36}$$

Numerical solution



The numerical solution for the current problem is achieved by following steps. 1. Conversion of momentum equation and continuity Eq. (1–3) into vorticity-streamfunction-based Eq. 2. The obtained vorticity-streamfunction equation along with energy equation is coupled with no-slip and temperature boundary conditions. 3. The coupled equations are discretized using the finite difference method and arranged implicitly. 4. The algebraic equations are attained in a tridiagonal manner and are solved using a tridiagonal matrix algorithm. The detailed procedure to generate the solution is illustrated in the following flow chart.

With the above procedure, the numerical algorithm is compared with the previously published problems in terms of streamfunction, isotherms and irreversibility analysis [47]. Figure 2 displays four plots arranged in the order of streamfunction, isotherm, irreversibility caused by heat transfer, and fluid friction from left to right. The arrangement of these plots is indicative of the similarity between the current study and previously published results, which prompted the initiation of this study.

Following this, the current is study to simulate the NCF within a TC using the FORTRAN algorithm. The algorithm is communicated with the initial and boundary conditions (25–27) to get a desired solution. After the evaluation of grid sensitivity test, the total number of grids is set to 14,884 nodes. Moreover, the distance between each node is considered as constant. The outcome of various grid is tabulated in Table 2. The main criteria for the selection of 14,884

Table 2 Grid sensitivity test ($Da = 10^{-2}$, $Ra = 10^6$ and $Ha = 5$)

Grid size	Nu	Time for convergence/s
1764(42 × 42)	10.7145	1381
3844(62 × 62)	10.9162	2721
6724(82 × 82)	11.1028	4502
10404(102 × 102)	11.3096	6631
14884(122 × 122)	11.3117	10120
20164(142 × 142)	11.3161	12368
26244(162 × 162)	11.3198	15674

nodes is the comparison of Nu and the time required for convergence.

Results and discussion

In order to enhance the thermal management in the EV's battery cell module, the cavities are attached to its casing in order to achieve natural convection heat transfer process. For the same, the NCF, heat transport and entropy generation within the cavity is analyzed using the streamfunction, temperature distribution, heatline and entropy generation contours along with the plots such as Nusselt number, Bejan number, cup mixing temperature and root-mean-square deviation of temperature, respectively. The analysis is done

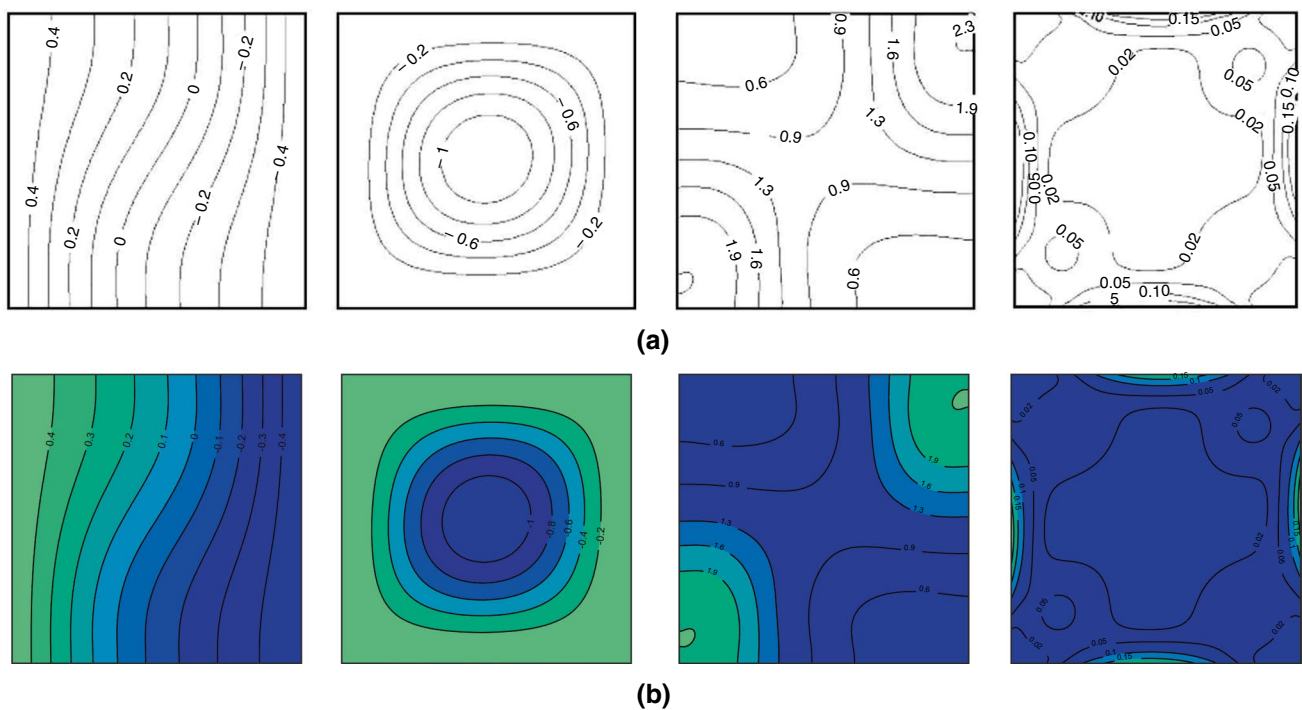


Fig. 2 Validation of algorithm

with the variation of volume fraction of the nanoparticles ($0.01 \leq \phi \leq 0.04$, to understand the effects of nanoparticles on NCF), Rayleigh number ($10^3 \leq Ra \leq 10^6$, to understand the buoyancy effects during convection), Darcy number ($10^{-5} \leq Da \leq 10^{-1}$, to find the effect of porosity), Hartman number ($0 \leq Ha \leq 50$, to find the magnetic effects) and amplitude ratio ($0.0 \leq A_r \leq 0.9$, to find the effects on NCF during the intensity of sinusoidal temperature), respectively.

Effect of amplitude ratio on NCF with respect to permeability

Figure 3 illustrates the contours of ψ , θ , Π , S_θ and S_ψ for Al_2O_3 -water nanofluid (denoted using dash line), Cu-water nanofluid (denoted using dash-dotted line) and Cu- Al_2O_3 -water hybrid nanofluid (denoted using solid line). The contours are picturized for the various values of Darcy number during $A_r = 0.0$, $Ra = 10^6$, $Ha = 5$ and

$\phi = 2\%$. In Fig. 3a, corresponding to $Da = 10^{-5}$, a smooth circulation of ψ is observed with a maximum of $\psi = -0.4$. In particular, two circulations are observed with the primary circulation of higher magnitude and a secondary circulation of very minor magnitude. The temperature distribution is allotted as per A_r , and linear variation is noticed toward the inclined wall. With respect to the velocity and temperature distribution, the heatfunction initiates from the left wall and dissipates toward the inclined cool wall. Here, the orientation of isotherms and heatfunction are in a perpendicular manner and thus illustrate the conduction domination. The entropy generated within the TC is higher at the left corner due to the shifting of temperature from high to low. Moreover, the entropy generation due to fluid friction is higher near the wall where maximum temperature occurs and lower portion of the inclined wall. It is noticed that the fluid friction irreversibility is less near the adiabatic wall. While increasing permeability by

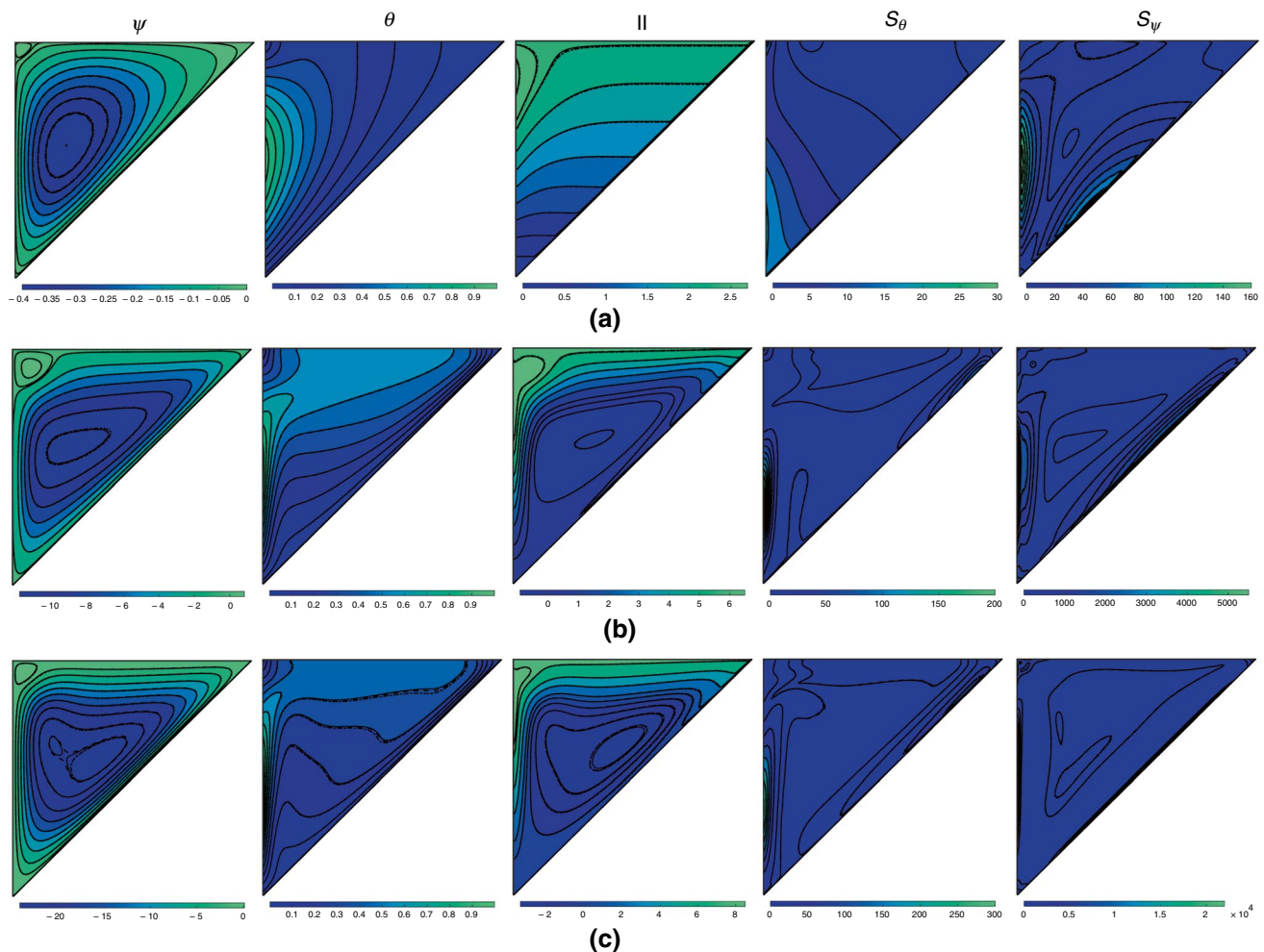


Fig. 3 Contour representation of ψ , θ , Π , S_θ and S_ψ for Al_2O_3 -water (dash), Cu-water (dash-dotted) and Cu- Al_2O_3 -water (solid) nanofluid **a** $Da = 1/10^5$, **b** $Da = 1/10^3$ and **c** $Da = 1/10^1$ at $A_r = 0.0$, $Ra = 10^6$, $Ha = 5$ and $\phi = 2\%$

magnifying Da to 10^{-3} , Fig. 3b leads to the streamline's circulation wider than the lower permeability stage (at the middle) and the secondary circulation also improves. The improved secondary circulation is due to the optimum permeability and the respective thermal boundary. During the selection of A_r to 0.0 provides the higher range of temperature slope along the boundary from $\theta = 0.0$ to 1.0. In regard to that, the temperature distribution also deviated from the boundary. The heat transport initiates from the left wall and maximum at the center. It is found that the heat flow from the center portion is distributed toward the inclined wall and upper portion of the left wall. There is a circulation in the middle of the heatlines contour and this illustrates the presence of convection. Also, during this permeability stage, S_θ is maximum near to lower half of the left boundary and next at the upper half of the inclined

wall. But, the maximum value of S_ψ is at the middle of the left wall and it is noted that the generation of fluid friction entropy is increased along the inclined wall. In middle of the S_ψ contour, there is a circulation also noted. Increasing Da to 10^{-1} leads to more permeability with a separation of streamfunction in the middle, where the maximum eddy is noticed. Apart from this, during lower values of Da , the circulation and other contours show lesser variation between Al_2O_3 -water, Cu-water and Cu- Al_2O_3 -water nanofluid. But, at $Da = 10^{-1}$ stage, Cu- Al_2O_3 -water hybrid nanofluid shows a higher value of ψ as compared to other normal nanofluids. With respect to wider spread streamfunction circulation, the isotherm widens and orthogonal to the boundary at the middle. The heatlines adjacent to the left wall are denser and its intense circulation denotes

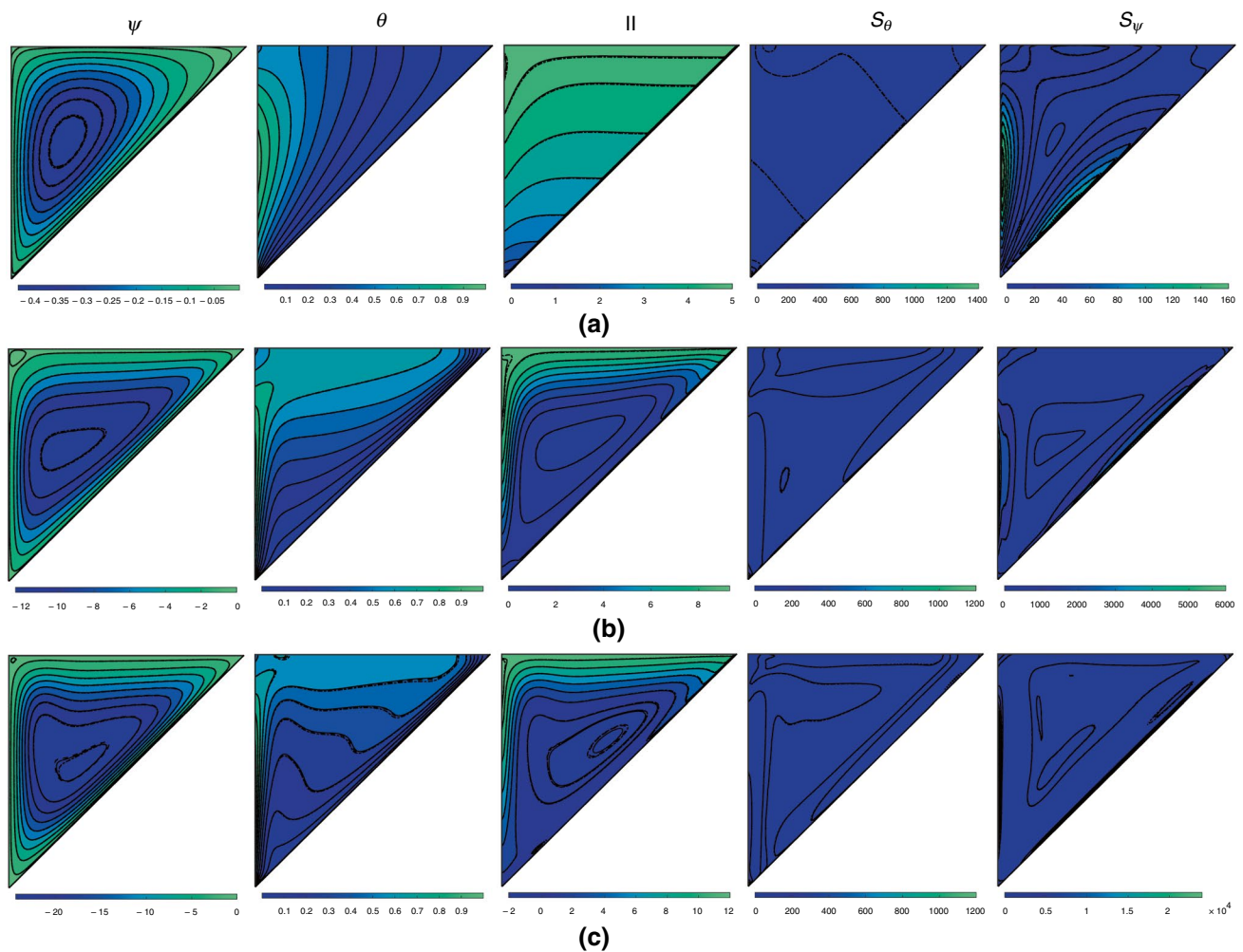


Fig. 4 Contour representation of ψ , θ , Π , S_θ and S_ψ for Al_2O_3 -water (dash), Cu-water (dash-dotted) and Cu- Al_2O_3 -water (solid) nanofluid **a** $Da = 1/10^5$ **b** $Da = 1/10^3$ and **c** $Da = 1/10^1$ at $A_r = 0.5$, $Ra = 10^6$, $Ha = 5$ and $\phi = 2\%$

the convection flow. In addition, improving Da leads to an amplification of S_θ and S_ψ .

With an increased amplitude ratio of $A_r = 0.5$, sinusoidal heating at the wall is adjusted, and the corresponding NCF patterns are illustrated in Fig. 4. There is a smooth circulation that carries over the entire cavity, and there are no secondary circulations are generated as compared to the case $A_r = 0.0$. But, the patterns of primary circulation are similar to the previous case when $Da = 10^{-5}$. Since there is no secondary circulation, isotherms experiences linear variation of temperature from the boundary toward the inclined wall. As per the primary circulation, the heat-line pattern is also defined orthogonal with the isotherms at lower permeability. However, there is a huge change in entropy generation is spotted; for instance, $|S_\theta|_{\max}$ improves from 30 to 1400. This is due to the wall's thermal boundary. However, there is a minor variation found in entropy generation with respect to fluid friction. When

Da is increased from 10^{-5} to 10^{-3} , the maximum value of S_θ reduces. However, the maximum value of S_ψ improves. The heatfunction also improves with permeability, based on the streamfunction intensity. Interestingly, it is noted that secondary circulation is generated. The intensity of this generated secondary circulation decreases with a further increase in the value of Da to 10^{-1} . During this stage, the convection has more impact on TC due to the improvement in permeability and higher Ra . In addition, the variation in ψ , θ and Π for Al_2O_3 -water, Cu -water and $Cu-Al_2O_3$ -water nanofluid are more at higher permeability conditions. In the case of entropy, Fig. 3b, c shows a minor change in the maximum value of S_θ . However, there is an exorbitant variation in fluid friction irreversibility.

An increment of A_r to 0.9 leads to the sinusoidal temperature boundary with less gradient and the corresponding contours of ψ , θ , Π , S_θ and S_ψ are depicted

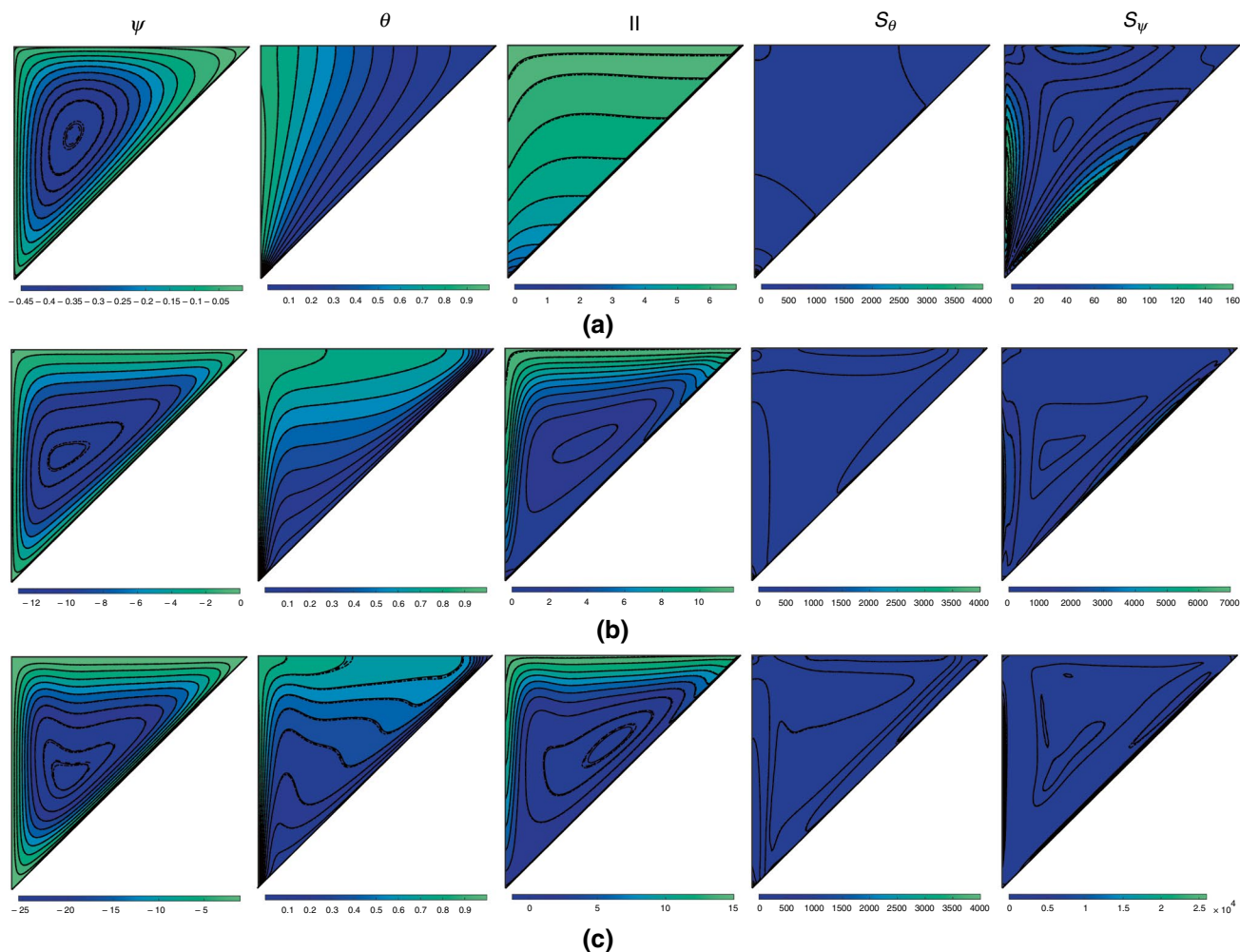


Fig. 5 Contour representation of ψ , θ , Π , S_θ and S_ψ for Al_2O_3 -water (dash), Cu -water (dash-dotted) and $Cu-Al_2O_3$ -water (solid) nanofluid a $Da = 1/10^5$, b $Da = 1/10^3$ and c $Da = 1/10^1$ at $A_r = 0.9$, $Ra = 10^6$, $Ha = 5$ and $\phi = 2\%$

in Fig. 5. As depicted, at $Da = 10^{-5}$, there is an improved circulation with the maximum intensity of $\psi_{\max} = -0.45$ is noted and there is no formation of secondary circulation as compared to the previous case. Also, there is a notable change is visible in the streamfunction contours of Al_2O_3 -water, Cu-water and Cu- Al_2O_3 -water nanofluid. It is noted that Al_2O_3 -water nanofluid's inner ψ circulation is less than the circulation with Cu-water nanofluid, while the inner circulation of Cu- Al_2O_3 -water hybrid nanofluid lies between both. With respect to this thermal boundary, there is a gradual reduction in temperature toward the inclined wall. Similar to the previous case, there is a horizontal-based heatlines orthogonal to the isotherms, indicating pure conduction. At this stage, the entropy generated with respect to heat transfer is more at the bottom sharp corner and it is magnified to $|S_\theta|_{\max} = 4000$ as compared to the case $A_r = 0.5$. Moreover, there is a minor variation noted in the S_ψ contour. While increasing Da to 10^{-3} , the maximum value of S_θ remains unchanged and only the value of S_ψ magnified to $|S_\psi|_{\max} = 7000$. The maximum fluid friction irreversibility is found adjacent to a center of the left and inclined wall. In ψ contour, still there is no secondary circulation, and only wider, intense primary circulation occurs. As per the streamfunction, isotherms are also aligned. Upon increasing the value of Da to 10^{-1} , the streamlines further get intense and bend in the middle. The isotherm makes a horizontal path in the middle. Additionally, the isotherm line runs parallel near the left wall and inclined wall, respectively. As a combination of streamfunction and isotherm, the heatlines are generated intensely near the left wall with the presence of circulation at the center. In addition, there is no change in S_θ with changing permeability. However, there is an intense change in the maximum value of fluid friction irreversibility ($|S_\psi|_{\max} > 25,000$).

Effect of Rayleigh number on NCF

Figure 6 illustrates the variation of contours ψ , θ , Π , S_θ and S_ψ due to the increment in Ra (ranged from 1000 to 1,000,000) when placing Cu- Al_2O_3 -water hybrid nanofluid in a TC at $A_r = 0.5$, $Da = 10^{-2}$, $Ha = 5$ and $\phi = 0.02$. At lower values of $Ra(10^3)$, there is smooth primary circulation within the entire TC with the absence of a secondary one. At this stage, the effect of buoyancy is minimal. Such that primary circulation gets the maximum circulation of $|\psi| \approx 0.18$. The temperature also reaches its maximum at the center and distributes linearly toward the inclined wall. An orthogonal-oriented heatline that is detected against the isotherms, illustrating the absence of convection transport. The maximum entropy, $|S_\theta|_{\max} = 1400$ at the lower corner

of the cavity and $|S_\psi|_{\max} = 0.3$ adjacent to an inclined wall of the cavity. While increasing the Ra to 10^4 , there is an enhancement in S_ψ , reaching a maximum value of $|S_\psi|_{\max} = 25$. But, there is no improvement or decrement in S_θ . As the Rayleigh number is hiked, there is a small distortion in the linearly varying temperature. Also, there is a distortion in the heatline with no circulation. This again shows the absence of convection. In the case of streamfunction contour, there is a formation of secondary circulation. While further increasing the value of Ra to 10^5 leads to the growth of both primary and secondary circulation, respectively. An effect due to buoyancy improves and the molecular density reduces. This makes the primary circulation and the respective sinusoidal boundary is responsible for the secondary circulation. The isotherms also bend at the mid-region, and there is a formation of heatline circulation. The circulation in the heatline denotes the presence of convection heat transfer as well. There is a minor change in the S_θ pattern and the maximum value is still unchanged. However, the maximum value of S_ψ raises to 1000 and the maximum value is found adjacent to the left and inclined walls. The maximum value is further enhanced to 18,000, when $Ra = 10^6$. However, there is a reduction in the generation of entropy with respect to heat transfer, i.e., $|S_\psi|_{\max}$ falls to 1200. If looking into the streamfunction plot, there is a descent in secondary circulation and quantification in the intensity of primary circulation occurs. At the center of TC, there is a bending in wider circulation and the same effects are reflected in both the temperature distribution and heat flow contour. Moreover, the intensity of heat transport is enhanced due to the force of buoyancy.

Effect of volume fraction of hybrid nanofluid on NCF

The summation of Cu- Al_2O_3 hybrid nanoparticles (volume fraction, ϕ) ranging from 1% to 4% in water during MHD-NCF, and their effects are illustrated through contours ψ , θ , Π , S_θ and S_ψ in Fig. 7. The plots are picturized during $A_r = 0.5$, $Ra = 10^6$, $Da = 1/10^2$ and $Ha = 5$. The changes within each contour with respect to ϕ are less as compared to other parameters. There is a small reduction in the circulation taking place while increasing ϕ and notably, the primary circulation bends in the middle. Thus, inner circulation during $\phi = 0.03$ bends and tries to shrink on the left side. And, this left part of the inner circulation region disappears on $\phi = 0.04$. The reduction in the circulation intensity is due to the addition of nanoparticles, which enhances the viscosity within the TC. An improved viscosity causes the flow to resist. However, the maximum value of heatlines is improved. This improvement is made by the thermophysical property (especially the thermal conductivity) of Cu and Al_2O_3 nanoparticles, respectively.

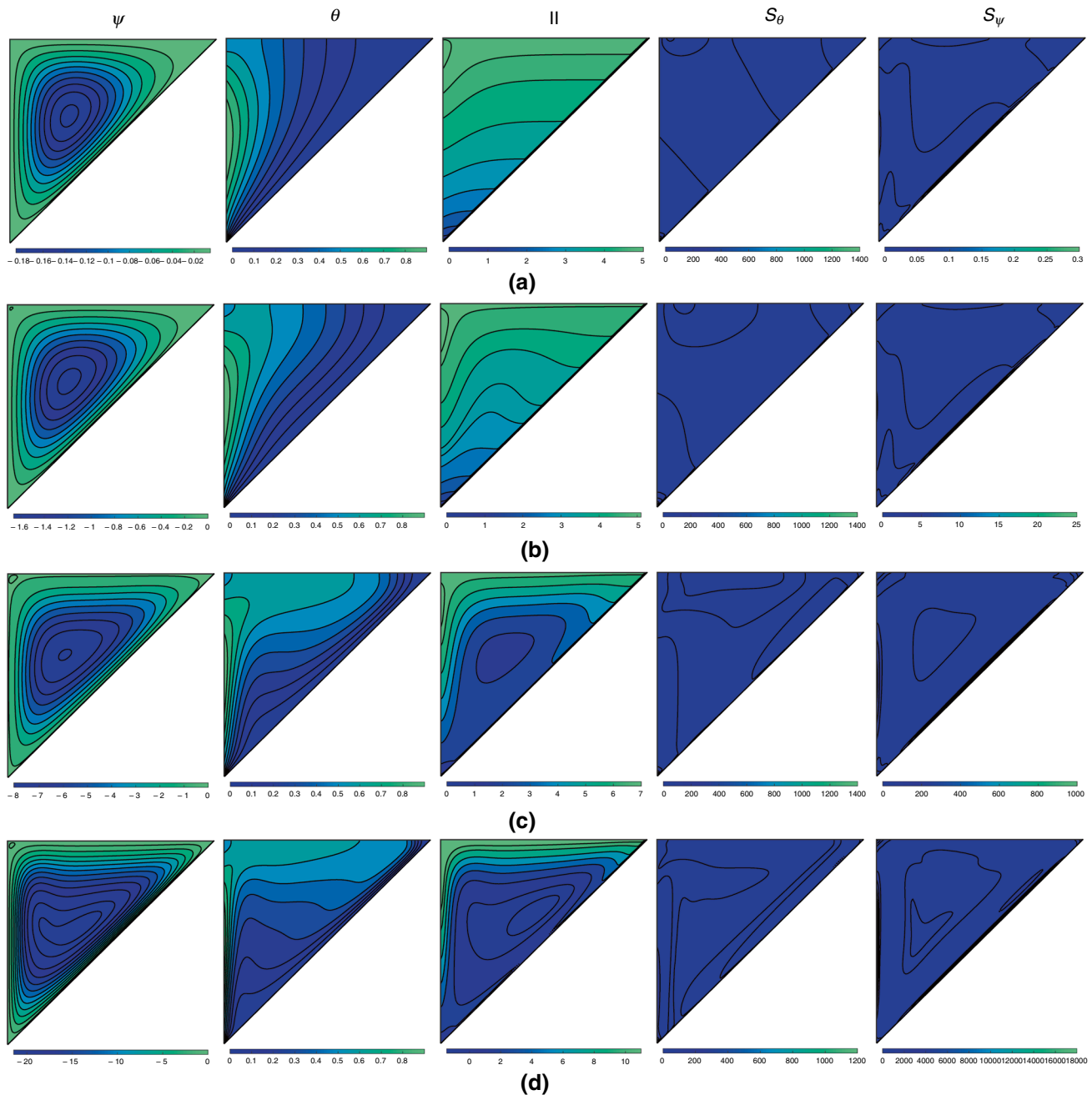


Fig. 6 Contour representation of ψ , θ , Π , S_θ and S_ψ for **a** $Ra = 10^3$ **b** $Ra = 10^4$ **c** $Ra = 10^5$ and **d** $Ra = 10^6$ during $A_r = 0.5$, $Da = 1/10^2$, $Ha = 5$ and $\phi = 2\%$

The heatlines circulation reduces but the value of Π_{\max} improves with ϕ . This denotes the quantification of conduction by distortion of convection. The maxima of S_θ improves while increasing ϕ from 0.01 to 0.02. However, there is no change in $|S_\theta|_{\max}$ when ϕ ranges from 0.02 to 0.04. Alternatively, the maximum value of S_ψ declines by changing ϕ from 0.01 to 0.02, and there are no changes in $|S_\psi|_{\max}$ by increasing the value of ϕ to 0.03 and 0.04.

Effect of applied magnetic field on NCF with respect to permeability

Figures 8 and 9 denote the contours of ψ , θ , Π , S_θ and S_ψ during the presence and absence of an applied magnetic field over the cavity for lower and higher permeability conditions. The intensity of the applied magnetic strength is enhanced using the non-dimensional parameter Ha , set

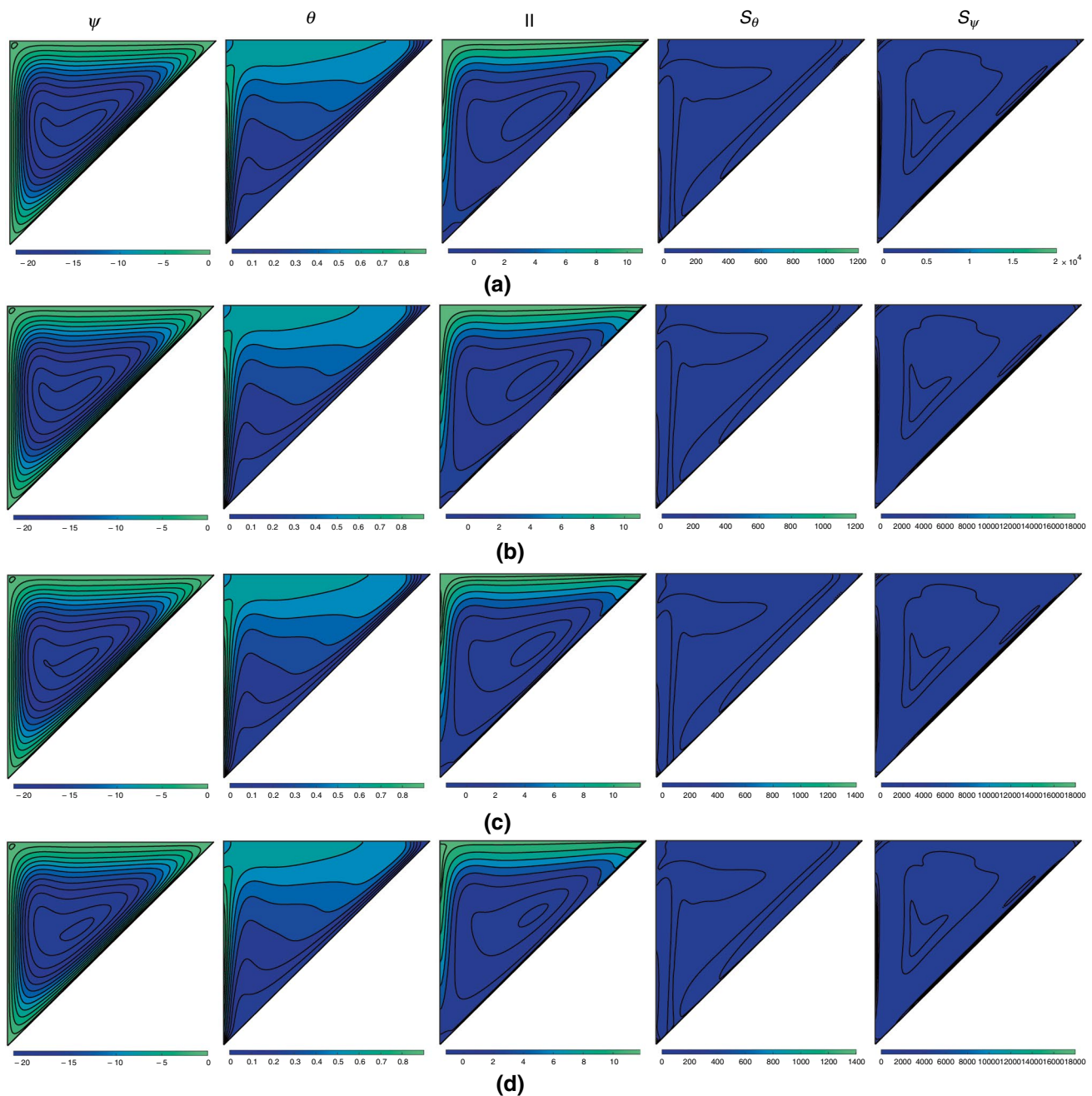


Fig. 7 Contour representation of ψ , θ , Π , S_θ and S_ψ for **a** $\phi = 1\%$ **b** $\phi = 2\%$ **c** $\phi = 3\%$ and **d** $\phi = 4\%$ during $A_r = 0.5$, $Da = 1/10^2$ and $Ha = 5$

to 25 and 50. These contours are depicted when $A_r = 0.5$, $Ra = 10^6$ and $\phi = 2\%$. Figure 7 shows the effects of Ha during lower permeability, and Fig. 8 shows the effects of Ha during higher permeability. While increasing the value of Ha , there is a fall in the swirling of streamlines. The circulations are here affected by the Lorentz force. This reduction rate of streamline intensity is less the lower value of Da , while the reduction of streamfunction intensity is more for higher permeability conditions. The temperature distribution has a minor effect during lower

Da , the horizontal nature of lines at the center of TC gets distorted and aligns inclined to the left wall. At lower permeability, curviness is present in the middle of the heatline during the absence of a magnetic field. This curviness is affected by increasing the value of Ha . However, there is an intense circulation present in the heatline at higher permeability, and this circulation is affected by the applied magnetic field. In addition, the value of Π_{\max} is reduced with higher values of Ha . The entropy generated due to heat transfer improves with the applied magnetic field

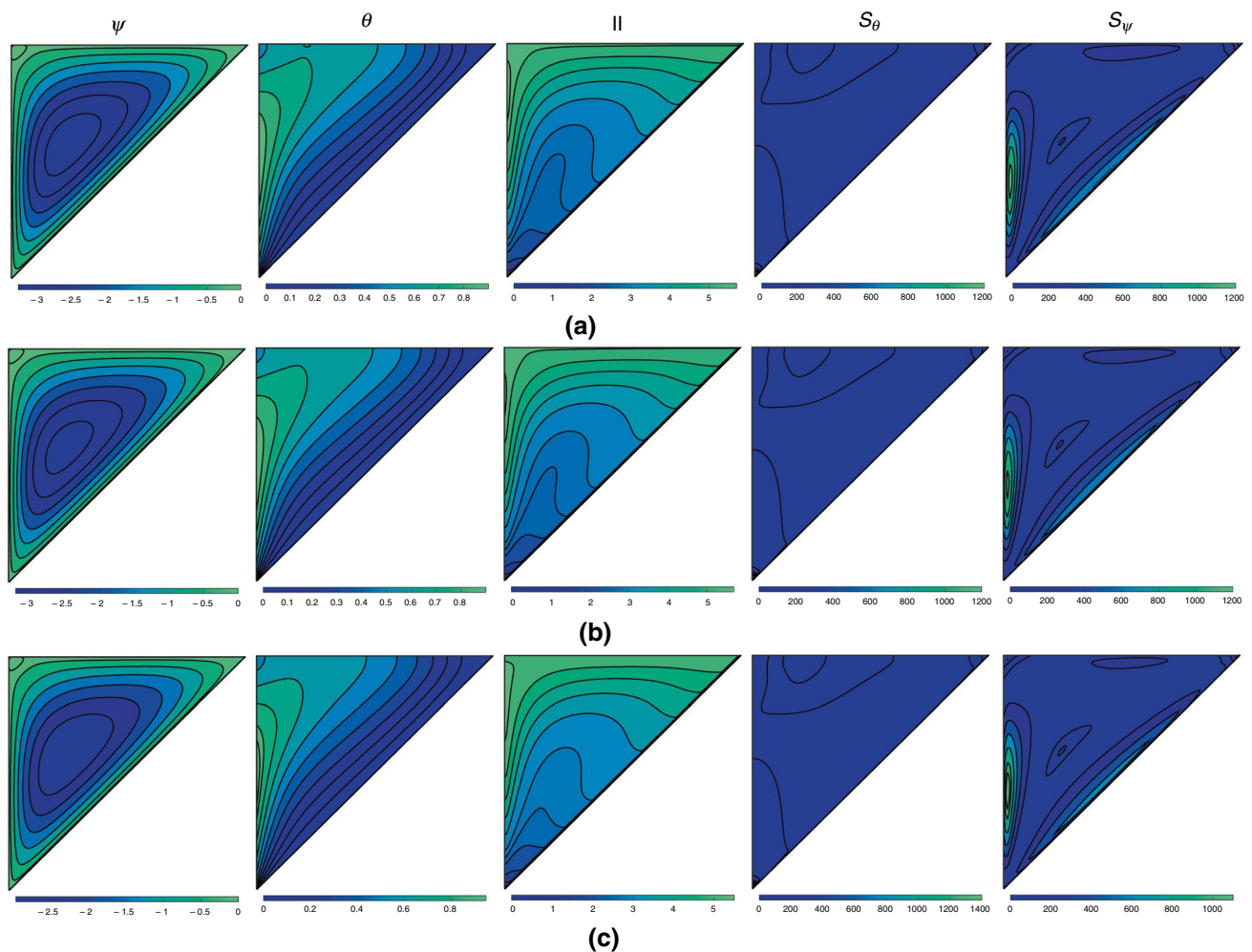


Fig. 8 Contour representation of ψ , θ , Π , S_θ and S_ψ for **a** $Ha = 0$, **b** $Ha = 25$ and **c** $Ha = 50$ during $A_r = 0.5$, $Ra = 10^6$, $Da = 1/10^4$ and $\phi = 2\%$

during lower permeability, with no notable change during higher values of Da with respect to the applied magnetic field. However, the entropy due to fluid friction is reduced by quantifying the strength of an applied magnetic field. The range of entropy reduction during lower permeability is very less as compared to the reduction during higher permeability. Precisely, $|S_\psi|_{\max}$ decreases from 1200 to 1000 during lower permeability and $|S_\psi|_{\max}$ decreases from 20000 to 5500 during higher permeability.

Heat transfer and entropy generation analysis of Cu–Al₂O₃–water hybrid nanofluid

Apart from the flow contours, the variation of Nu , Be , Θ_{cup} and \mathfrak{R} for Cu–Al₂O₃–water hybrid nanofluid with respect to A_r , Ra , Ha and Da are depicted in Fig. 10. The surface plots are marginated to amplitude ratio along one direction, the fixed variables Da , Ha and Ra along one direction and the derived Nu , Be , Θ_{cup} and \mathfrak{R} is illustrated along the

positive direction. Figure 10a shows that the quantification of permeability causes the heat transfer to fall and magnifies during lower A_r . However, the heat transfer continuously enhances during higher A_r . At lower value of A_r , the conduction dominates at $Da < 10^{-3}$. As the amplitude ratio improves, the convection effects are stimulated. Similar to Da , magnification of Ra leads to enhancement in Nu . Ultimately, due to the Lorentz force, an increase in the value of Ha makes a fall in Nu regardless of with A_r . A reverse behavior is noticed with the value of Be on improving the value of Ra , Da and Ha as illustrated in Fig. 10b. The fall in Be is significant when increasing the value of Da until 10^4 and a small reduction is found after $Da = 10^4$. Conversely, there is a continuous fall is noted with the value of Ra . The reduction in the value of Be with respect to Da and Ra denotes the distortion of entropy generation with respect to heat transfer. However, there is a growth in heat transfer irreversibility happens while increasing the value of Ha . The main reason behind this is the Lorentz force retarding the motion and the

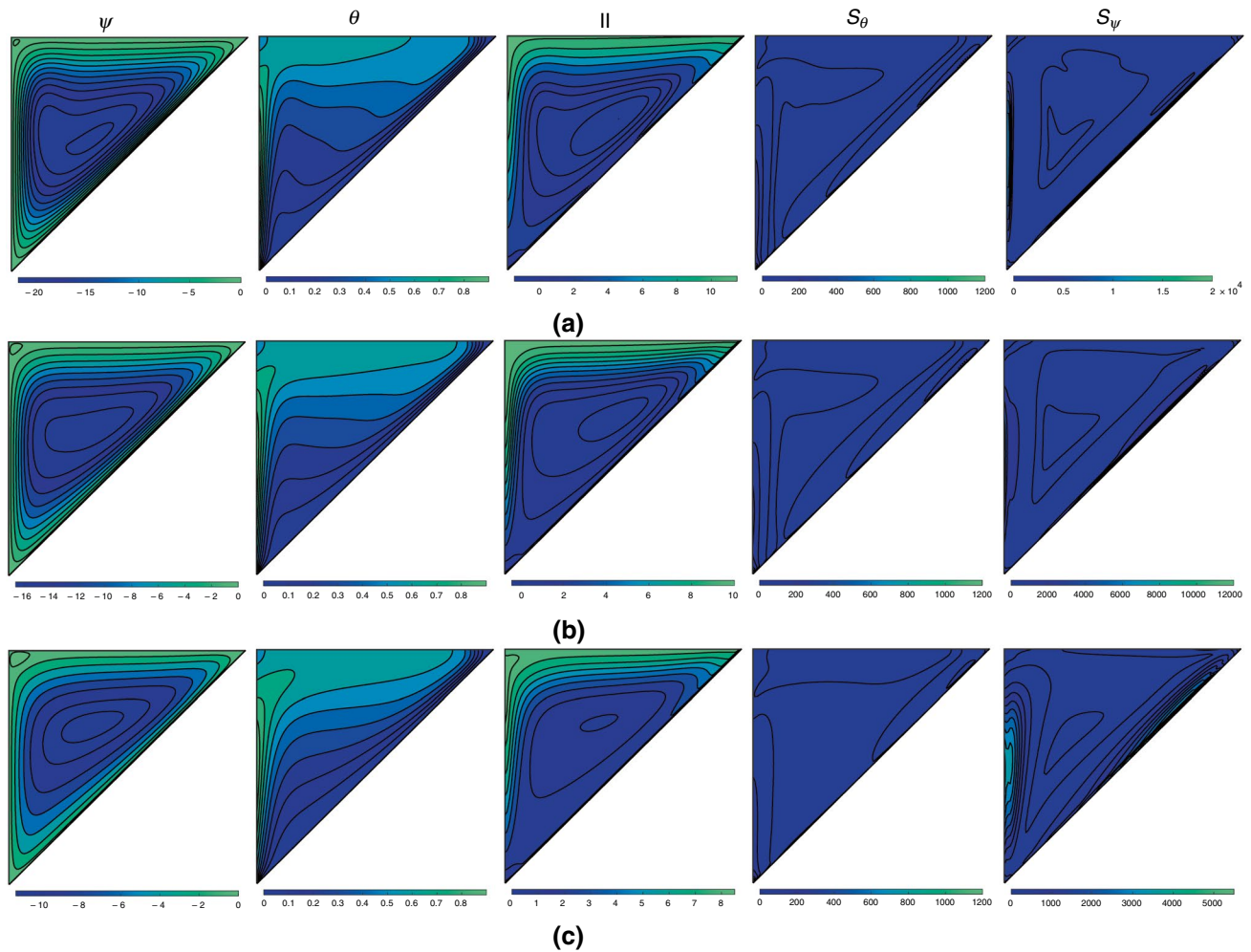


Fig. 9 Contour representation of ψ , θ , Π , S_θ and S_ψ for **a** $Ha = 0$, **b** $Ha = 25$ and **c** $Ha = 50$ during $A_r = 0.5$, $Ra = 10^6$, $Da = 1/10^2$ and $\phi = 2\%$

subsequent decrease in convection. As a result, the conduction domination improves.

The change in velocity-weighted average temperature with respect to Ra , Da , Ha and A_r is highlighted in Fig. 10c. It is observed that Θ_{cup} rises from $Da = 10^{-5}$ to $Da = 10^{-4}$, indicating a conduction-dominated temperature distribution below $Da = 10^{-4}$. Further on $Da > 10^{-3}$, there is a fall in Θ_{cup} . The mixing temperature is improved with respect to buoyancy force. A similar behavior happens on increasing the value of Ra . During the augmentation of Ra , the cup mixing temperature increases until $Ra = 10^5$, after which further increase in Ra leads to a reduction in Θ_{cup} . This illustrates that convection-based mixing temperature occurs above $Ra = 10^5$. Conversely, there is a distortion of convection-based mixing temperature occurs while increasing the effect of an applied magnetic field. Eventually, the degree of temperature uniformity with respect to change in Ra , Da , Ha and A_r is highlighted in Fig. 10d.

The lower the \mathfrak{R} value, higher the temperature uniformity. The temperature uniformity reduces until $Da = 10^{-4}$ for every value of A_r . Beyond this value of Da , there is an improvement in temperature uniformity. The temperature uniformity is high in the case of higher-order non-uniformity boundary conditions. Similarly, the temperature uniformity with respect to convection heat/fluid flow improves at $Ra > 10^5$. On the contrary, there is a reduction in the temperature uniformity or an increase in the value of \mathfrak{R} occurs with the applied magnetic field strength.

Comparison of heat transfer and entropy generation of normal and hybrid nanofluid

The comparison of Nu , Be , Θ_{cup} and \mathfrak{R} for Cu- Al_2O_3 -water, Al_2O_3 -water and Cu-water nanofluid with respect to change in Da , Ra and Ha is depicted in Fig. 11a-c. The figure is depicted when $Ra = 10^6$, $Da = 10^{-2}$, $A_r = 0.5$. As the figure denotes, Nu is high or

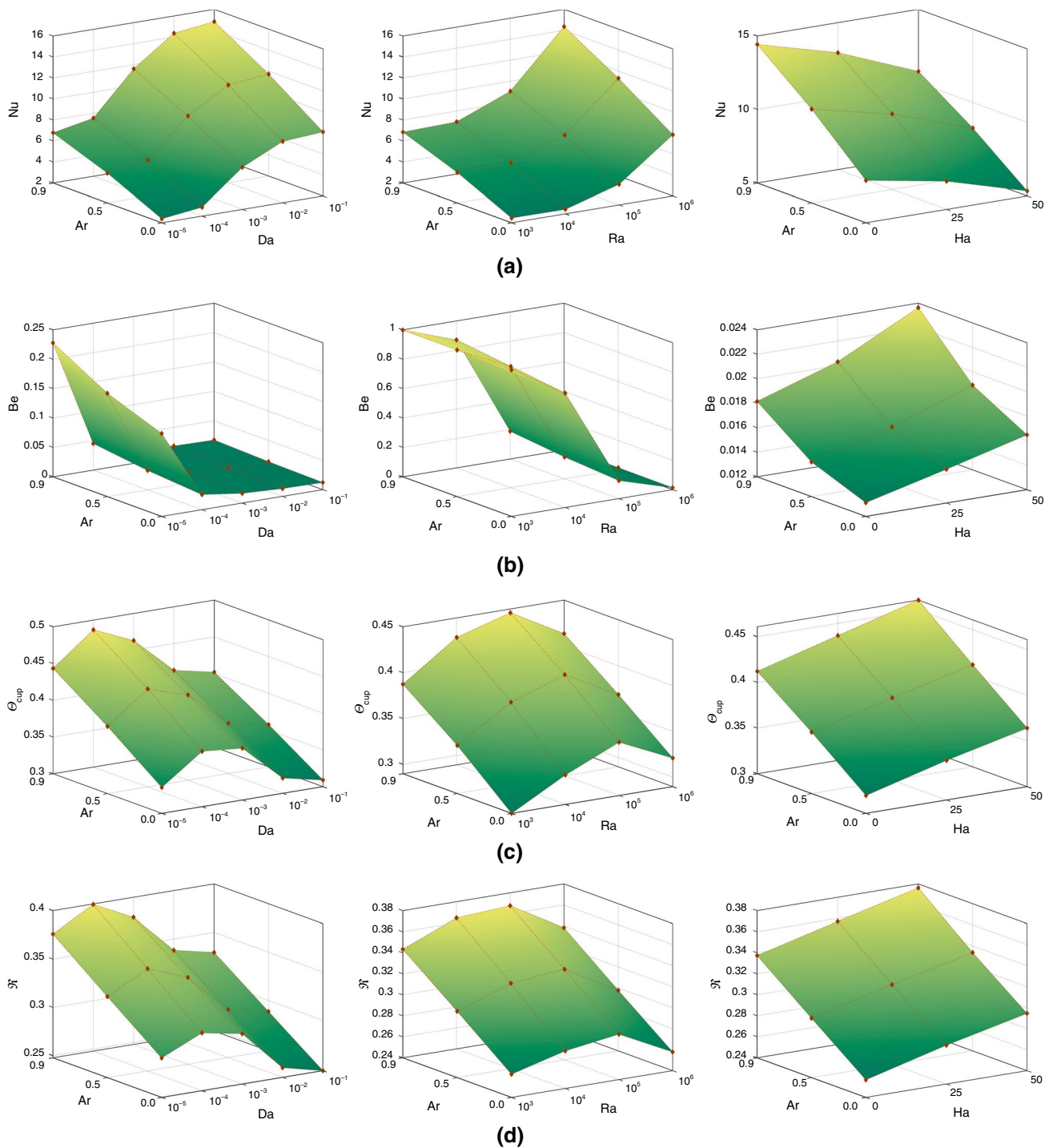


Fig. 10 Variation of Nu , Be , Θ_{cup} and \mathfrak{R} for Cu–Al₂O₃–water nanofluid with respect to Ar , Ra , Ha and Da

dominated by Cu–water nanofluid until $Da = 10^{-3}$ and during $Da > 10^{-3}$, Cu–Al₂O₃–water nanofluid's heat transfer is higher than the other normal nanofluid. The same trend occurs with increasing values of Ra . Until $Ra = 10^5$, heat transport by Cu–water nanofluid dominates and

when $Ra = 10^6$, heat transfer by Cu–Al₂O₃–water hybrid nanofluid is superior. Thus, at higher values of Ra and Da , Cu–Al₂O₃–water hybrid nanofluid's heat transfer is high, and Al₂O₃–water nanofluid's heat transfer is low. It is noted that the overall heat release of nanofluids is

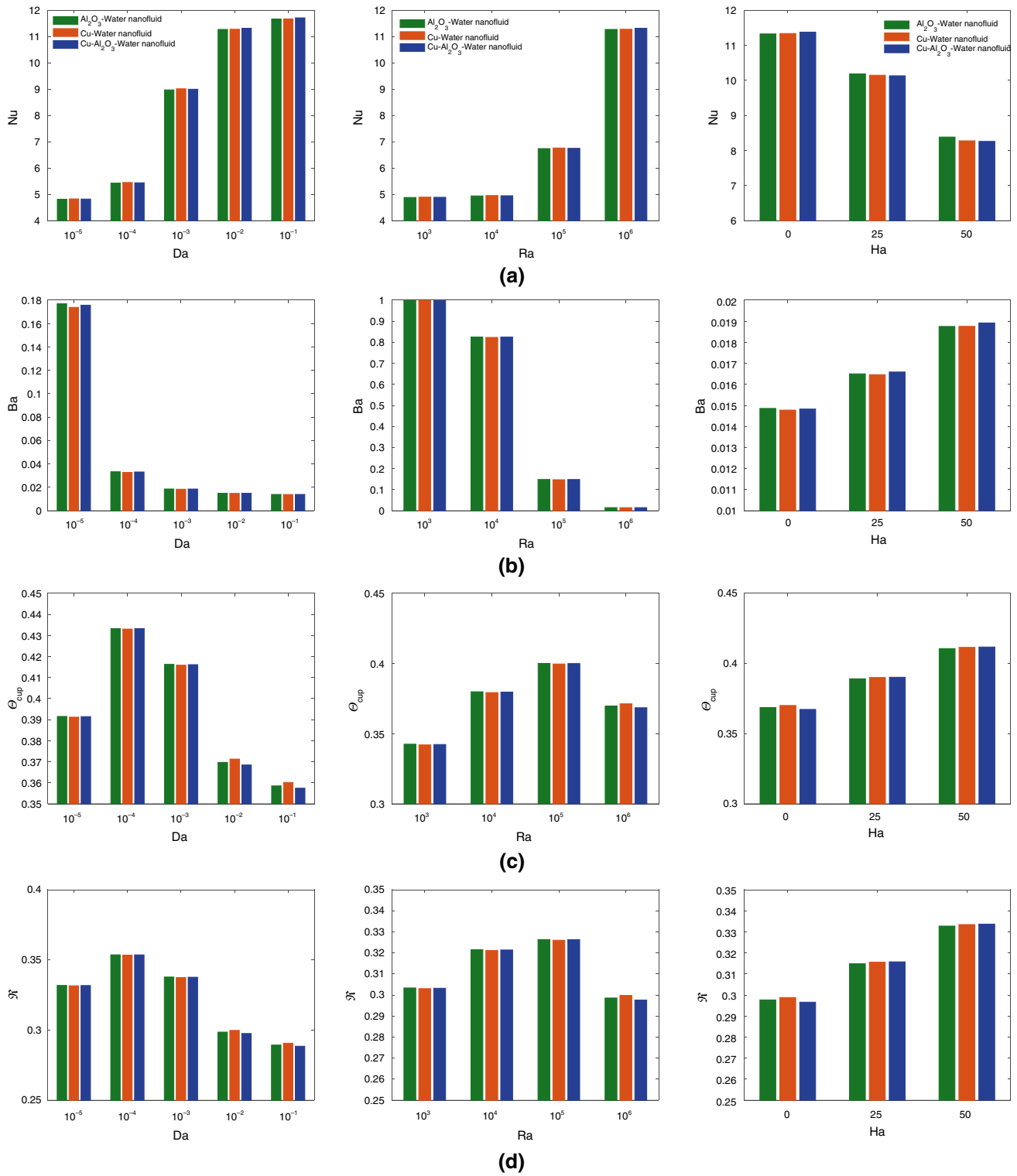


Fig. 11 Variation of Nu, Be, Θ_{cup} and \mathfrak{I} for Al₂O₃-water, Cu-water and Cu-Al₂O₃-water nanofluid with respect to Ha, Ra and Da

influenced by the Lorentz force. Upon increasing the value of Ha to 25 and 50, the heat discharge rate is more affected to Cu-Al₂O₃-water nanofluid only. Under these conditions, the maximum heat transfer is by Al₂O₃-water and

lesser heat transfer by Cu-Al₂O₃-water hybrid nanofluid, respectively. It is known that irreversibility declines as the heat release rate increases. When the value of Da is increased, fall in Be is observed. Specifically, the value

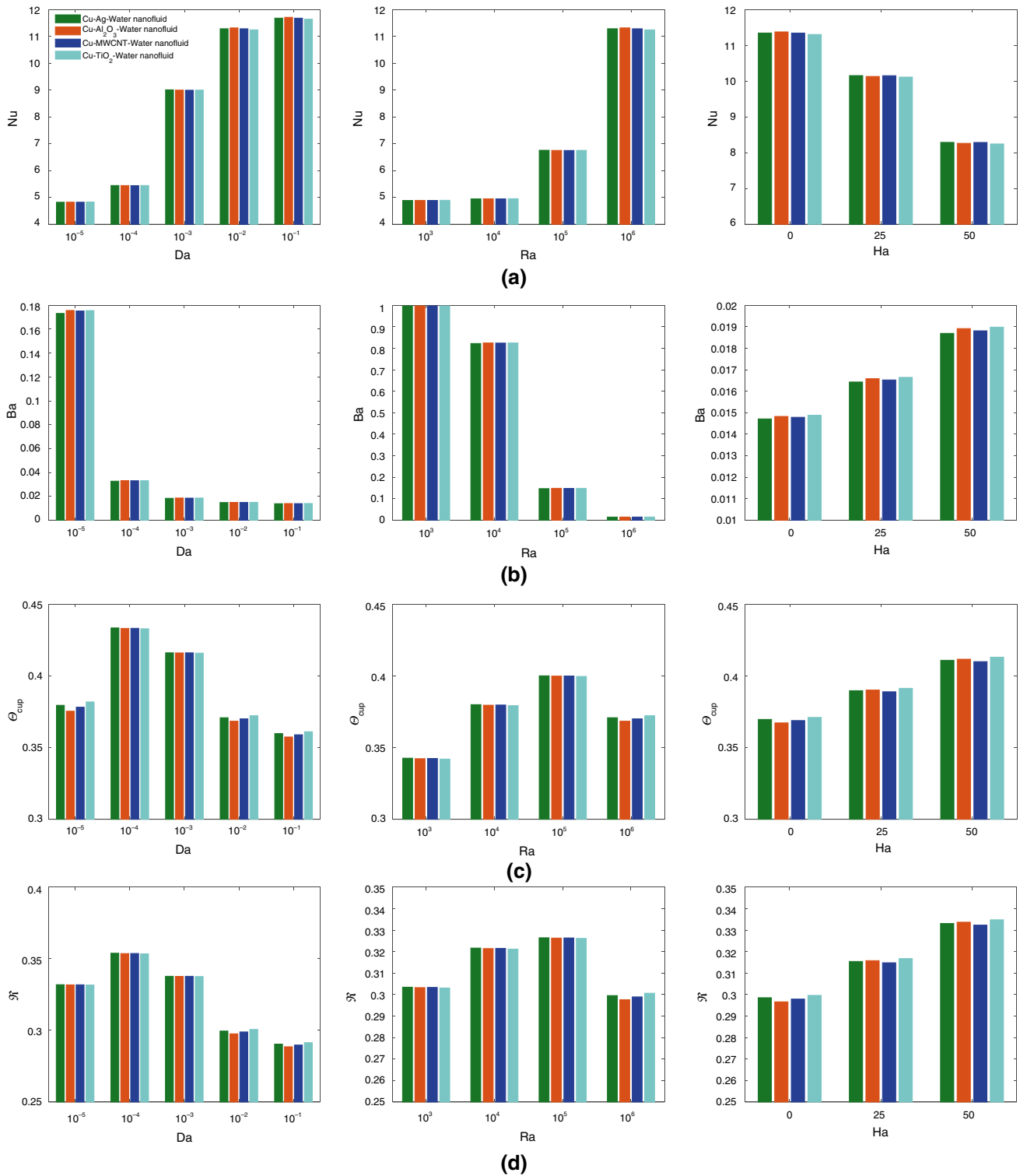


Fig. 12 Variation of Nu , Be , Θ_{cup} and \mathfrak{R} for Cu–Ag–water, Cu–Al₂O₃–water, Cu–MWCNT–water and Cu–TiO₂–water nanofluid with respect to Ha , Ra and Da

of Be is higher for Al₂O₃–water nanofluid and lower for Cu–water nanofluid at $Da = 10^{-5}$. However, at $Da = 10^{-1}$, there is a minor change in the Be for all the nanofluids. In

particular, the Cu–Al₂O₃–water nanofluid’s Bejan number value is slightly less than the Cu–water nanofluid. There is a significant variation spotted on the values of Be for

varying the values of Ra . Although there is a minor variation between the nanofluids. On increasing the values of Ha , Cu–Al₂O₃–water nanofluid provides higher Be .

The thermal mixing due to convection improves with higher values of Ra and Da . It is noted that at higher Darcy numbers and Rayleigh numbers, thermal mixing is superior for Cu–Al₂O₃–water nanofluid, followed by Al₂O₃–water nanofluid. However, thermal mixing is poorer for the Cu–water nanofluid. On the other side, the thermal mixing of Al₂O₃–water nanofluid is better over others during higher values of Ha . Similarly, on higher Ha , temperature uniformity is enhanced for Al₂O₃–water nanofluid. In the absence of a magnetic field and during higher values of Ra and Da , Cu–Al₂O₃–water nanofluid exhibits better temperature uniformity.

Comparison of heat transfer and entropy generation among various hybrid nanofluids

The study is repeated to analysis changes in Nu , Be , Θ_{cup} and \mathfrak{R} by using various combinations of Cu–water-based hybrid nanofluids. These combinations include Cu–Ag–water, Cu–Al₂O₃–water, Cu–MWCNT–water and Cu–TiO₂–water hybrid nanofluid respectively. Figure 12 is generated under the condition of $Ra = 10^6$, $Da = 10^{-2}$, $\phi = 0.02$, $A_r = 0.5$ and $Ha = 5$ as a base value. At lower Da values, heat transfer by all the hybrid nanofluids is similar. However, at higher Da values, Cu–Al₂O₃–water hybrid nanofluid provides higher Nu , followed by Cu–Ag–water, Cu–MWCNT–water and Cu–TiO₂–water hybrid nanofluids, respectively. A similar trend is followed in case of varying the Rayleigh number. At non-presence of the applied magnetic field, the order of heat transfer for hybrid nanofluids follow a similar pattern as at the higher values of Da and Ra . On applying the magnetic field, especially at $Ha = 50$, the value of Nu is higher for Cu–Ag–water nanofluid, followed by Cu–MWCNT–water, Cu–Al₂O₃–water and Cu–TiO₂–water hybrid nanofluids, respectively.

The Be is highest for Cu–Al₂O₃–water nanofluid when $Da = 10^{-5}$ and followed by Cu–TiO₂–water, Cu–MWCNT–water and Cu–Ag–water nanofluids, respectively. However, there is only a minor variation among different hybrid nanofluids at higher Darcy numbers. Similarly, at higher Da values in combination with higher Ra values, Cu–TiO₂–water nanofluid exhibits the highest Be , followed by Cu–Al₂O₃–water, Cu–MWCNT–water and Cu–Ag–water nanofluids, respectively. In addition, it is found that the previous order is emphasized when increasing the value of Ha to 25 and 50. The value of Θ_{cup} is high for Cu–TiO₂–water nanofluid and less for Cu–Al₂O₃–water at lower values of Da . On the other hand, during Darcy number equal to 10^{-4} and 10^{-3} , cup mixing temperatures of all the

hybrid nanofluids look similar. At higher values of Da , again Cu–TiO₂–water nanofluid provides highest Θ_{cup} , followed by Cu–Ag–water, Cu–MWCNT–water and Cu–Al₂O₃–water hybrid nanofluids, respectively. This trend persists at $Ra = 10^6$ and in the absence of a magnetic field. When Ha is increased, only Cu–Al₂O₃–water hybrid nanofluid raises, while the other nanofluids remain in the same order. The temperature uniformity is similar in all the hybrid nanofluids during lower Da and Ra values. However, as Ra and Da increase, Cu–TiO₂–water nanofluid provides highest \mathfrak{R} value, followed by Cu–Ag–water, Cu–MWCNT–water and Cu–Al₂O₃–water hybrid nanofluids, respectively. This order is affected by increasing the intensity of the applied magnetic field. At $Ha = 25$ and 50 , Cu–Al₂O₃–water hybrid nanofluid provides the highest \mathfrak{R} value next to the Cu–TiO₂–water hybrid nanofluid.

Conclusions

The electric vehicle (EV) battery plays a crucial role in making sustainable transport. An effective thermal management of the battery is necessary to ensure its better efficiency and longevity. Thus, the study aims to enhance the thermal management of battery cell modules by incorporating a series of cavities attached to the casing. Heat transfer from the battery cell modules is improved through free convection facilitated by the cavities. To achieve this, the heat generated within the battery cell module casing (assumed heat is not-uniform and the sinusoidal heating with a function of amplitude ratio, A_r), is transferred using cavities filled with various hybrid nanofluids. The various hybrid nanofluids used in the study are Cu–Al₂O₃–water, Cu–Ag–water, Cu–MWCNT–water and Cu–TiO₂–water hybrid nanofluid.

The outcomes are evaluated using metrics such as velocity-weighted average temperature, root-mean-square deviation, Bejan and Nusselt numbers, streamlines, heatlines, isotherms and entropy generation. Some notable outcomes of the study are,

- The temperature uniformity due to convection improves during higher permeability and higher buoyancy effect. On the contrary, temperature uniformity is disturbed by the intensity of an applied magnetic field.
- It is found that Cu–Al₂O₃–water-based hybrid nanofluid delivers a higher heat transfer rate as compared to Cu–water and Al₂O₃–water normal nanofluids during higher Ra and Da .

- In addition, it is found that at higher values of Ra and Da, Cu–Al₂O₃–water hybrid nanofluid outperforms other hybrid nanofluids in providing a higher heat transfer rate.
- While applying and improving the intensity of the applied magnetic field, the Lorentz force resist the heat flow, leading to a reduction in convection heat transfer rate. Especially, Cu–Al₂O₃–water and Cu–TiO₂–water hybrid nanofluids exhibit lower heat transfers as compared to other hybrid and normal nanofluids.
- The irreversibility with respect to fluid friction increases with an improvement in permeability and buoyancy effect. Conversely, fluid friction irreversibility reduces with the applied magnetic field. In addition, heat transfer irreversibility increases with the addition of ϕ .
- In the case of increasing the amplitude ratio of sinusoidal heating in the wall, the overall heat release rate is increased. For instance, at higher values of Da, Ra and A_r, a 68% increase in the Nusselt number occurs with a right-angled inverted TC as compared to the square cavity [41].

From the study, it is concluded that utilizing an inverted right-angled TC filled with Cu–Al₂O₃–water hybrid nanofluid along with the battery cell module improves thermal management through natural convection, particularly when battery module casing experiences sinusoidal heating as a function of amplitude ratio. Moreover, the application of an external magnetic field is not recommended, as the Lorentz force resists the convection heat transfer rate, especially, the heat transfer by Cu–Al₂O₃–water hybrid nanofluid.

Acknowledgements None

Author contribution AVK, AJC, and SD contributed to framing the mathematical model of the problem and participated in the discussion of results. LJ conducted the numerical computations and obtained the results. AsJ, EM, SAS and AJ reviewed earlier literature and contributed to the Introduction section. LJ verified the discussion of results and conducted technical writing. All authors participated in reviewing and proofreading the manuscript.

Declarations

Conflict of interest None.

References

1. Chen K, Chen Y, Li Z, Yuan F, Wang S. Design of the cell spacings of battery pack in parallel air-cooled battery thermal management system. *Int J Heat Mass Transf*. 2018.
2. Katoch SS, Eswaramoorthy M. A detailed review on electric vehicles battery thermal management system. *IOP Conf Ser Mater Sci Eng*. 2020. <https://doi.org/10.1088/1757-899X/912/4/042005>.
3. Wang M, Hung T-C, Xi H. Numerical study on performance enhancement of the air-cooled battery thermal management system by adding parallel plates. *Energies*. 2021. <https://doi.org/10.3390/en14113096>.
4. Zhang J, Wu X, Chen K, Zhou D, Song M. Experimental and numerical studies on an efficient transient heat transfer model for air-cooled battery thermal management systems. *J Power Sources*. 2021.
5. Bejan A. *Convection heat transfer*. Wiley; 2013.
6. Buchberg H, Catton I, Edwards DK. Natural convection in enclosed spaces: a review of application to solar energy collection. *J Heat Transf*. 1976;98:182–8.
7. Burmeister LC. *Convective heat transfer*. Wiley; 1993.
8. Krishna MV, Chamkha AJ. Hall and ion slip effects on unsteady MHD convective rotating flow of nanofluids: application in biomedical engineering. *J Egypt Math Soc*. 2020. <https://doi.org/10.1186/s42787-019-0065-2>.
9. Ribbens CJ, Watson LT, Wang CY. Steady viscous flow in a triangular cavity. *J Comput Phys*. 1994. <https://doi.org/10.1006/jcph.1994.1090>.
10. Varol Y, Oztop HF, Mobedi M, Pop I. Visualization of natural convection heat transport using heatline method in porous non-isothermally heated triangular cavity. *Int J Heat Mass Transf*. 2008. <https://doi.org/10.1016/j.ijheatmasstransfer.2008.04.023>.
11. Basak T, Aravind G, Roy S. Visualization of heat flow due to natural convection within triangular cavities using Bejan's heatline concept. *Int J Heat Mass Transf*. 2009. <https://doi.org/10.1016/j.ijheatmasstransfer.2008.10.034>.
12. Kaluri RS, Anandalakshmi R, Basak T. Bejan's heatline analysis of natural convection in right-angled triangular enclosures: effects of aspect-ratio and thermal boundary conditions. *Int J Therm Sci*. 2010. <https://doi.org/10.1016/j.ijthermalsci.2010.04.022>.
13. Krishna MV, Bharathi K, Chamkha AJ. Hall effects on MHD peristaltic flow of jeffrey fluid through porous medium in a vertical stratum. *Interfacial Phenom Heat Transf*. 2018. <https://doi.org/10.1615/InterfacPhenomHeatTransfer.2019030215>.
14. Krishna MV, Jyothi K, Chamkha AJ. Heat and mass transfer on MHD flow of Second grade fluid through porous medium over a semi-infinite vertical stretching sheet. *J Porous Media*. 2020. <https://doi.org/10.1615/JPorMedia.2020023817>.
15. Krishna MV, Anand PVS, Chamkha AJ. Heat and mass transfer on free convective flow of micropolar fluid through a porous surface with inclined magnetic field and hall effects. *Spec Top Rev Porous Media*. 2019. <https://doi.org/10.1615/SpecialTopicsRevPorousMedia.2018026943>.
16. Krishna MV, Swarnalathamma BV, Chamkha AJ. Investigations of Soret, Joule and Hall effects on MHD rotating mixed convective flow past an infinite vertical porous plate. *J Ocean Eng Sci*. 2019. <https://doi.org/10.1016/j.joes.2019.05.00>.
17. Krishna MV. Hall and ion slip effects and chemical reaction on MHD rotating convective flow past an infinite vertical porous plate with ramped wall and uniform wall temperatures. *Biomass Convers Biorefinery*. 2022. <https://doi.org/10.1007/s13399-022-03160-2>.
18. Basak T, Roy S, Ramakrishna D, Pop I. Visualization of heat transport during natural convection within porous triangular cavities via heatline approach. *Numer Heat Transf Part A Appl*. 2010. <https://doi.org/10.1080/10407780903507866>.
19. Yesiloz G, Aydin O. Laminar natural convection in right-angled triangular enclosures heated and cooled on adjacent walls. *Int J Heat Mass Transf*. 2013. <https://doi.org/10.1016/j.ijheatmasstransfer.2013.01.009>.
20. Nazir MW, Javed T, Ali N, Nazeer M. Effects of radiative heat flux and heat generation on magnetohydrodynamics natural convection flow of nanofluid inside a porous triangular cavity with thermal

- boundary conditions. *Numer Methods Partial Differ Equ.* 2021. <https://doi.org/10.1002/num.22768>.
21. Varol Y, Oztop HF, Koca A. Entropy production due to free convection in partially heated isosceles triangular enclosures. *Appl Therm Eng.* 2008. <https://doi.org/10.1016/j.applthermaleng.2007.08.013>.
 22. Varol Y, Oztop HF, Pop I. Entropy generation due to natural convection in non-uniformly heated porous isosceles triangular enclosures at different positions. *Int J Heat Mass Transf.* 2009. <https://doi.org/10.1016/j.ijheatmasstransfer.2008.08.026>.
 23. Basak T, Anandalakshmi R, Gunda P. Role of entropy generation during convective thermal processing in right-angled triangular enclosures with various wall heatings. *Chem Eng Res Des.* 2012. <https://doi.org/10.1016/j.cherd.2012.03.008>.
 24. Bhardwaj S, Dalal A, Pati S. Influence of wavy wall and non-uniform heating on natural convection heat transfer and entropy generation inside porous complex enclosure. *Energy.* 2015. <https://doi.org/10.1016/j.energy.2014.11.036>.
 25. Biswal P, Basak T. Entropy generation vs energy efficiency for natural convection based energy flow in enclosures and various applications: a review. *Renew Sustain Energy Rev.* 2017. <https://doi.org/10.1016/j.rser.2017.04.070>.
 26. Rashidi S, Yang L, Khoosh-Ahang A, Jing D, Mahian O. Entropy generation analysis of different solar thermal systems. *Environ Sci Pollut Res.* 2020. <https://doi.org/10.1007/s11356-020-08472-2>.
 27. Choi SUS, Eastman JA. Enhancing thermal conductivity of fluids with nanoparticles. *ASME Internarional Mech Eng Congr Expo.* 1995.
 28. Buongiorno J. Convective transport in nanofluids. *J Heat Transf.* 2006. <https://doi.org/10.1115/1.2150834>.
 29. Sheikholeslami M, Ganji DD. Applications of nanofluid for heat transfer enhancement. *Appl Nanofluid Heat Transf Enhanc.* 2017;1–605.
 30. Krishna MV, Chamkha AJ. Hall effects on MHD squeezing flow of a water-based nano-fluid between two parallel disks. *J Porous Media.* 2019. <https://doi.org/10.1615/JPorMedia.2018028721>.
 31. Wong KV, De Leon O. Applications of nanofluids: current and future. *Adv Mech Eng.* 2010. <https://doi.org/10.1155/2010/519659>.
 32. Basak T, Chamkha AJ. Heatline analysis on natural convection for nanofluids confined within square cavities with various thermal boundary conditions. *Int J Heat Mass Transf.* 2012. <https://doi.org/10.1016/j.ijheatmasstransfer.2012.05.025>.
 33. Sheremet MA, Pop I. Free convection in a triangular cavity filled with a porous medium saturated by a nanofluid. *Int J Numer Methods Heat Fluid Flow.* 2015. <https://doi.org/10.1108/HFF-06-2014-0181>.
 34. Redouane F, Jamshed W, Devi SSU, Prakash M, Nasir NAAM, Hammouch Z. Heat flow saturate of Ag/MgO-water hybrid nanofluid in heated trigonal enclosure with rotate cylindrical cavity by using Galerkin finite element. *Sci Rep.* 2022. <https://doi.org/10.1038/s41598-022-06134-6>.
 35. Bondareva NS, Sheremet MA, Oztop HF, Abu-Hamdeh N. Entropy generation due to natural convection of a nanofluid in a partially open triangular cavity. *Adv Powder Technol.* 2017. <https://doi.org/10.1016/j.apt.2016.09.030>.
 36. Al-Zamily AMJ. Analysis of natural convection and entropy generation in a cavity filled with multi-layers of porous medium and nanofluid with a heat generation. *Int J Heat Mass Transf.* 2017. <https://doi.org/10.1016/j.ijheatmasstransfer.2016.10.102>.
 37. Das D, Roy M, Basak T. Studies on natural convection within enclosures of various (non-square) shapes: a review. *Int J Heat Mass Transf.* 2017. <https://doi.org/10.1016/j.ijheatmasstransfer.2016.08.034>.
 38. Humnic G, Humnic A. Entropy generation of nanofluid and hybrid nanofluid flow in thermal systems: a review. *J Mol Liq.* 2020. <https://doi.org/10.1016/j.molliq.2020.112533>.
 39. Tayebi T, Öztop HF, Chamkha AJ. Natural convection and entropy production in hybrid nanofluid filled-annular elliptical cavity with internal heat generation or absorption. *Therm Sci Eng Prog.* 2020. <https://doi.org/10.1016/j.tsep.2020.100605>.
 40. Kumar AV, Lawrence J, Saravanakumar G. Fluid friction/heat transfer irreversibility and heat function study on MHD free convection within the MWCNT–water nanofluid-filled porous cavity. *Heat Transf.* 2022. <https://doi.org/10.1002/htj.22498>.
 41. Jino L, Kumar AV. MHD natural convection of hybrid nanofluid in a porous cavity heated with a sinusoidal temperature distribution. *Comput Therm Sci An Int J.* 2021. <https://doi.org/10.1615/ComputThermalSci.2021037663>.
 42. Swamy HAK, Sankar M, Reddy NK. Analysis of entropy generation and energy transport of Cu–Water nanofluid in a tilted vertical porous annulus. *Int J Appl Comput Math.* 2022. <https://doi.org/10.1007/s40819-021-01207-y>.
 43. Kaluri RS, Basak T. Entropy generation due to natural convection in discretely heated porous square cavities. *Energy.* 2011. <https://doi.org/10.1016/j.energy.2011.06.001>.
 44. Ghasemi B, Aminossadati SM, Raisi A. Magnetic field effect on natural convection in a nanofluid-filled square enclosure. *Int J Therm Sci.* 2011. <https://doi.org/10.1016/j.ijthermalsci.2011.04.010>.
 45. Mansour MA, Siddiqa S, Gorla RSR, Rashad AM. Effects of heat source and sink on entropy generation and MHD natural convection of Al₂O₃–Cu/water hybrid nanofluid filled with square porous cavity. *Therm Sci Eng Prog.* 2018. <https://doi.org/10.1016/j.tsep.2017.10.014>.
 46. Malik S, Nayak AK. MHD convection and entropy generation of nanofluid in a porous enclosure with sinusoidal heating. *Int J Heat Mass Transf.* 2017. <https://doi.org/10.1016/j.ijheatmasstransfer.2017.03.123>.
 47. Ilis GG, Mobedi M, Sunden B. Effect of aspect ratio on entropy generation in a rectangular cavity with differentially heated vertical walls. *Int Commun Heat Mass Transf.* 2008. <https://doi.org/10.1016/j.icheatmasstransfer.2008.02.002>.
 48. Mehrez Z, El Cafsi A, Belghith A, Le Quére P. MHD effects on heat transfer and entropy generation of nanofluid flow in an open cavity. *J Magn Magn Mater.* 2015. <https://doi.org/10.1016/j.jmmm.2014.08.010>.

Publisher's Note Springer Nature remains neutral with regard to jurisdictional claims in published maps and institutional affiliations.

Springer Nature or its licensor (e.g. a society or other partner) holds exclusive rights to this article under a publishing agreement with the author(s) or other rightsholder(s); author self-archiving of the accepted manuscript version of this article is solely governed by the terms of such publishing agreement and applicable law.